Supplementary Information

Light-driven restructuring generates nanoisland NiIr alloy for efficient methane dry reforming.

Chengxuan He[1,2], Ruijie Yang[1,2], Chenggui Zhong[1,2], Zhicheng Ye[1,2], Yuan Dong[1,2], Weihao Chen[1,2], Lingyun Chen[1,2], Zhihan Wang[1,2], Shiqun Wu[1,2]*, and Jinlong Zhang[1,2]*

[1] Key Laboratory for Advanced Materials, Joint International Research Laboratory of Precision Chemistry and Molecular Engineering, Feringa Nobel Prize Scientist Joint Research Center, School of Chemistry and Molecular Engineering, East China University of Science & Technology, Shanghai 200237, China

[2] Shanghai Engineering Research Center for Multi-media Environmental Catalysis and Resource Utilization, East China University of Science and Technology, Shanghai 200237, China

*Correspondence: wushiqun@ecust.edu.cn

*Correspondence: jlzhang@ecust.edu.cn

This PDF file includes:

Supplementary Methods
Supplementary Notes 1 to 7
Supplementary Figs. 1 to 45
Supplementary Tables 1 to 5
Supplementary References 1 to 28

Supplementary Methods

Characterization. Aberration-corrected high-angle annular dark-field scanning transmission electron microscopy (HAADF-STEM, FEI-Themis Z) images were recorded using a convergence semi angle of 11 mrad, and inner- and outer collection angles of 59 and 200 mrad, respectively. Energy mapping and energy-dispersive X-ray spectroscopy (EDS) were conducted using four Super-X detectors integrated into the column. Powder X-ray diffraction (XRD) patterns were acquired on a Rigaku D/MAX 2550 diffractometer with Cu Kα radiation (λ=1.5406 Å) operated at 40 KV and 40 mA, scanning 2θ angles from 10° to 80°. Raman spectroscopy was performed on a Renishaw in Via system using a 532 nm laser excitation source. UV-Vis-NIR diffuse reflectance spectra were recorded on a Varian Cary 500 spectrophotometer equipped with an integrating sphere, using $BaSO_4$ as a reference. Inductively coupled plasma atomic emission spectrometry (ICP-AES, Varian 730-ES, Agilent) quantified the metal loadings of catalysts. Thermogravimetric analysis (TGA) of spent catalysts was conducted on a Netzsch STA 449 F5 analyzer under air flow (50 mL min^{-1}), heating from 100 ºC to 800 ºC at 10 ºC·min^{-1}. Temperature-programmed desorption (TPD) experiments were performed on an Auto Chem II 2920 (Micromeritics, USA) in pure He, ramping to 770 °C at 10 ºC·min^{-1}. H_2-O_2 titration was performed on a temperature programmed chemisorption analyzer (VDSorb-91i) to measure metal dispersion. Photoluminescence (PL) spectra were acquired at room temperature using a Cary Eclipse fluorescence spectrometer (Agilent). Femtosecond transient absorption (fs-TA) spectroscopy was performed on a Helios pump-probe system (Ultrafast Systems, USA) with an 800 nm Ti:sapphire laser (Coherent Legend, 85 fs pulse width, 1 kHz repetition rate). The pump beam (325 nm, 80 μW) was generated via frequency doubling in a β-barium borate (BBO) crystal, while the probe beam (near-infrared continuum) monitored photoexcited states. Isotope labeling experiments employed a high-precision gas isotope mass spectrometer (Nu Instruments Horizon, UK): a 1:1 mixture of CH_4 and $C^{18}O_2$ was introduced into a batch reactor in the dark, followed by 15-minute irradiation (300 W Xe lamp, 3.89 Wcm^{-2}). Reaction products were cryogenically separated and analyzed for $C^{16}O$ and $C^{18}O$ isotopes.

Electrochemical measurements. Electrochemical measurements were conducted at room temperature using a Zahner Zennium potentiostat (Zahner-elektrik GmbH, Germany) with a three-electrode configuration: a fluorine-doped tin oxide (FTO) working electrode, graphite counter electrode, and saturated calomel reference electrode (SCE). For working electrode preparation, 5 mg of catalyst was dispersed in 0.5 mL ethanol, and 20 μL of the slurry was drop-casted onto FTO (1 cm^2 active area) and dried under ambient conditions. Transient photocurrent responses were measured in N_2-saturated 0.5 M Na_2SO_4 under 300 W Xe lamp irradiation. Electrochemical impedance spectroscopy (EIS) was performed in a frequency range from 100 kHz to 0.1 Hz under amplitude of 10 mV using N_2 saturated potassium ferricyanide mixed electrolyte without Xe lamp irradiation.

Theoretical calculations. Density functional theory (DFT) calculations were implemented by materials studio and Vienna ab initio simulation package (VASP)[1,2]. Perdew-Burke-Ernzerhof (PBE) of the generalized gradient approximation (GGA) was employed to describe the exchange-correlation functional[3,4]. The cutoff energy for the plane-wave basis set was set to 400 eV, and the Monkhorst-Pack k-point sampling was generated with a 1×1×1 grid. The convergence criterion for the force was 0.05 eV/Å. The surface calculations were carried out using a 4× 4 slab

and the surface atoms were relaxed. The vacuum layer of 15 Å was introduced to avoid interactions between periodic images. The adsorption energy (eV) was defined as follows: $E_{ad} = E_{A\text{-}S} - (E_S + E_A)$, where $E_{A\text{-}S}$ is the energy of the slab together with the adsorbate, E_A is the total energy of the free adsorbate and E_S is the total energy of the bare slab. The d band center (ε_d) was calculated as follows:

$$\varepsilon_d = \int_{-\infty}^{+\infty} n_d(\varepsilon)\varepsilon d\varepsilon / \int_{-\infty}^{+\infty} n_d(\varepsilon) d\varepsilon.$$

Excitation-dependent charge redistribution calculations are performed with ORCA software[5]. The functional employed was PBE0, and the basis set used was def2-SVP. (This basis set is an all-electron basis set for the first four periods and a pseudopotential basis set starting from the fifth period, so no mixed basis set is required.) The electron-hole structures were calculated using Multiwfn[6], and the visualization data were obtained using the visual molecular dynamics VMD software[7].

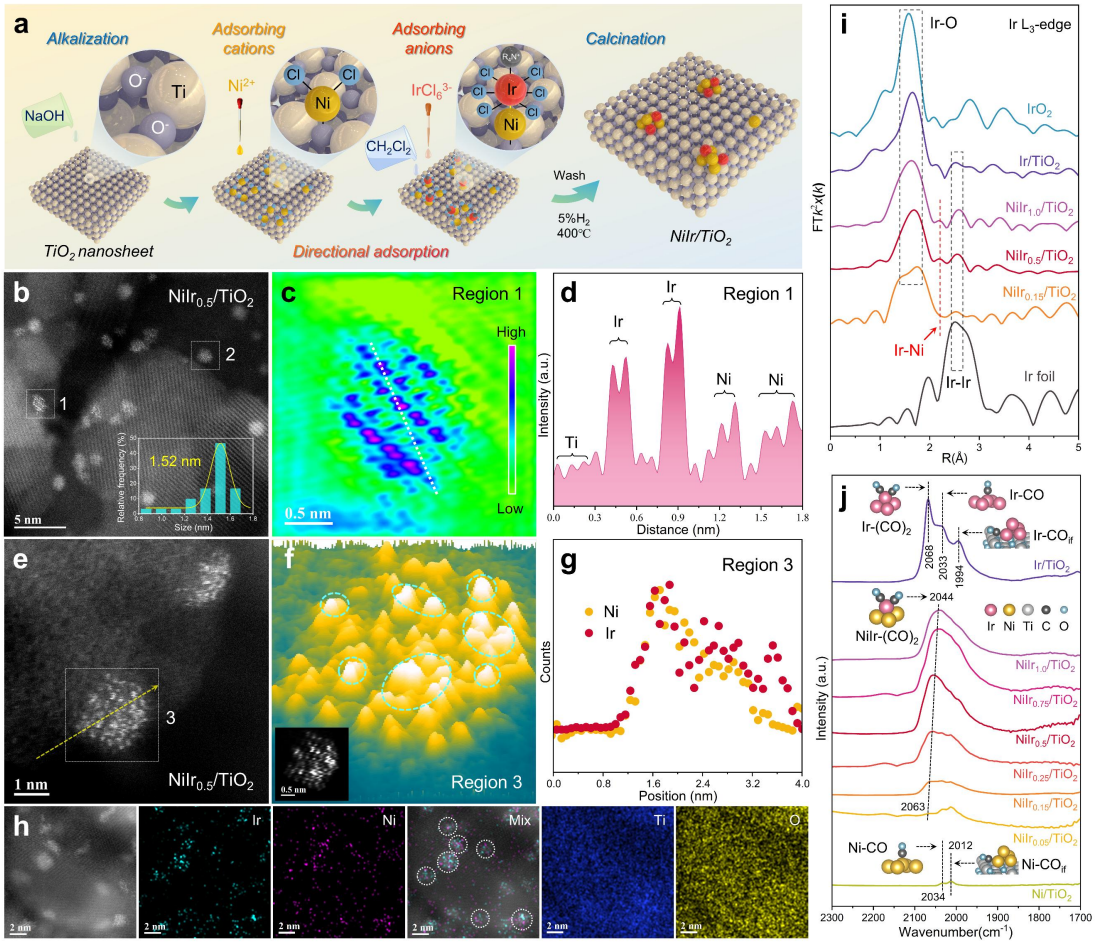

Supplementary Fig. 1. Synthesis and structural characterization of TiO_2-supported partially oxidized NiIr nanoclusters. (a) Schematic of the directional adsorption strategy for synthesizing NiIr nanoclusters supported on TiO_2. (b) Aberration-corrected HAADF-STEM image of $NiIr_{0.5}/TiO_2$ and cluster size distribution (inset). (c) Color-coded atomic map of region 1 (marked by the white dashed box in b**)** after image filtering. (d) Intensity profiles along the white line in c. (e) Aberration-corrected HAADF-STEM image of NiIr nanoclusters on TiO_2. (f) 3D surface plot with atomic overlapping region 3 in **e**. Blue dashed circles indicate the Ir atoms in NiIr nanocluster. Inset: Filtered image of region 3. (g) EDS line-scan profiles of Ni and Ir across a cluster along the yellow arrow in **e**. (h) HAADF-STEM image and corresponding EDS elemental mapping of $NiIr_{0.5}/TiO_2$. (i) k^2-weighted Fourier transform of Ir L_3-edge EXAFS spectra (without phase correction) for Ir foil, IrO_2, $NiIr_x/TiO_2$, and Ir/TiO_2. (j) *In situ* CO-probe DRIFTS spectra of $NiIr_x/TiO_2$, Ni/TiO_2, and Ir/TiO_2 at the 15th minute of Ar-flow during desorption (25 °C); schematic models of surface structures are included in j.

Supplementary Note 1. **Synthesis and atomic-scale structural analysis of partially oxidized NiIr nanoclusters on TiO_2.**

To construct bimetallic NiIr nanoclusters on TiO_2 with precise atomic pairing, we adopted a directional adsorption strategy[8] (Supplementary Fig. 1a; see Methods for synthesis details). This approach leverages sequential electrostatic adsorption of cationic Ni complexes and anionic Ir precursors onto alkalized TiO_2 nanosheets, ensuring preferential Ir anchoring onto pre-adsorbed Ni sites. By conducting the adsorption process in an aprotic solvent and introducing anionic Ir precursor complexed with quaternary ammonium, we minimized competitive adsorption of Ni and Ir, and effectively reduced metal leaching, which are common challenges in conventional co-impregnation methods. Subsequent H_2 calcination eliminated organic ligands while strengthening Ni-Ir metallic interactions, yielding ultrafine bimetallic clusters with uniform dispersion on the TiO_2 support (Supplementary Fig. 1b). Inductively coupled plasma-atomic emission spectrometry (ICP-AES) confirms controlled metal loadings across $NiIr_x/TiO_2$ samples (Supplementary Fig. 2, Table S1), where *x* denotes the Ir/Ni theoretical atomic ratio. The sublinear increase in Ir/Ni ratios with *x* suggests saturation of Ir adsorption onto pre-adsorbed Ni sites, excluding independent Ir deposition. For comparison, monometallic Ni/TiO_2 and Ir/TiO_2 were prepared with a theoretical loading of 1 wt.% for each metal. Aberration-corrected HAADF-STEM analysis revealed that Ni species or Ir species on TiO_2 exhibited sub-1.2 nm clusters (Supplementary Figs. 3-4), whereas the $NiIr_x$ nanoclusters on TiO_2 showed an increase in size, progressively reaching up to 1.61 nm with higher Ir content (Supplementary Figs. 5). This trend supports the co-stabilization of Ni and Ir atoms within the bimetallic clusters. This size evolution directly supports the formation of bimetallic NiIr nanoclusters, as the incorporation of Ir stabilizes the clusters and promotes their growth. Atomic-scale characterization of $NiIr_{0.5}/TiO_2$ provided further insights into the spatial distribution of Ni and Ir atoms. Filtered and color-coded HAADF-STEM images and the corresponding intensity profiles (Supplementary Fig. 1c-d, Supplementary Fig. 6b-c) revealed intertwined Ni-Ir distributions within individual clusters. The 3D surface plot of a selected region (Supplementary Fig. 1f) highlighted Ir atoms (whitish-yellow peaks within blue dashed marks) surrounding Ni atoms (darker yellow bumps), demonstrating cohesive bimetallic nanocluster formation. Conversely, monometallic samples exhibited only metal-TiO_2 contrast (Supplementary Figs. 3g-h, 4e-f). Moreover, EDS line scans (Supplementary Fig.1g) and elemental mapping (Supplementary Fig. 1h and Supplementary Fig. 6d-i) confirmed the intimate contact between Ni and Ir atoms. Owing to the higher atomic ratio of Ni to Ir, trace amounts of isolated Ni species inevitably persist. Crucially, all Ir atoms preferentially occupy Ni-associated sites, with no detectable isolated Ir single atoms observed on the TiO_2 support (Supplementary Fig. 1b).

Next, we elucidate the chemical structure and coordination environment of the NiIr nanoclusters. X-ray Diffraction (XRD) patterns confirm exclusive anatase-phase TiO_2 (Supplementary Fig. 7), with no detectable reflections from metallic Ni or Ir phases, consistent with HAADF-STEM evidence of dispersed sub-2 nm clusters. Normalized Ir L_3-edge and Ni K-edge X-ray absorption near-edge spectroscopy (XANES) analysis reveal partially oxidized states of Ni and Ir (Supplementary Fig.8a-b). Linear combination fitting (Supplementary Fig. 8c-d) shows higher Ir oxidation in Ir/TiO_2 (+3.6) than $NiIr_{0.5}/TiO_2$ (+2.7), and more reduced Ni in Ni/TiO_2 (+1.6) versus $NiIr_{0.5}/TiO_2$ (+1.8), indicating electron transfer from Ni to Ir, later corroborated by *in situ* analyses. Extended X-ray absorption fine structure (EXAFS) at the Ir

L_3-edge provides atomic-scale coordination details (Supplementary Fig. 1i). All samples exhibit a prominent peak at ~1.60 Å and a relatively weaker peak at ~2.56 Å, corresponding to Ir-O scattering and Ir-Ir scattering, respectively. Notably, $NiIr_x/TiO_2$ samples exhibit an additional peak at 2.18 Å, which can be attributed to Ni-Ir scattering. These results demonstrate that NiIr nanoclusters exhibit a partially oxidized state, with electronic modulation between Ni and Ir atoms. The partial oxidation probably arises from the interface reconstruction between nanocluster and the surface lattice O atoms of TiO_2 during the calcination process and the exposure to air during storage. This unique electronic structure, coupled with their ultrafine size, positions these partially oxidized NiIr nanoclusters (Ox-NiIr) as promising candidates for the adsorption of CH_4 and CO_2 due to their inherent thermal instability[9].

In situ CO probe molecule diffuse reflectance infrared Fourier transform spectroscopy (DRIFTS) analyses were conducted to unravel the surface structure and adsorption behavior of NiIr nanoclusters (Supplementary Fig. 9 and Supplementary Fig. 1j). Ni/TiO_2 exhibited negligible *CO chemisorption signals (<2100 cm^{-1}), which vanished entirely upon heating to 100 ℃. This confirms the inadequacy of individual Ni sites for CO adsorption. In contrast, Ir-containing samples ($NiIr_x/TiO_2$, Ir/TiO_2) display intense *CO chemisorption bands (2100-1990 cm^{-1}), with adsorption strength scaling with Ir content. Heating-up desorption revealed a volcanic trend: *CO intensity peaked at 200 ℃ and declined continuously to 400 ℃. It demonstrates reversible CO binding, which is a critical feature for sustaining DRM activity. Detailed comparison of the desorption spectra at 25 ℃ (Fig. 1j) highlights distinct Ir coordination environments. For Ir/TiO_2, three CO species were resolved: (i) multi-carbonyl Ir-$(CO)_2$ (2068 cm^{-1}, low-coordination sites)[10], (ii) linear CO on metallic Ir (Ir-CO, 2033 cm^{-1})[11], and (iii) bridged CO at Ir-TiO_2 interfaces (Ir_{if}-CO, 1994 cm^{-1})[12]. For Ni/TiO_2, only weak peaks of Ni-CO and Ni_{if}-CO can be observed. In $NiIr_x/TiO_2$, the dominant Ir-$(CO)_2$ peak progressively shifts downward (2063→2044 cm^{-1}) with increasing Ir content, signaling enhanced π-backdonation from Ir to CO. The observed redshift arises from Ni-to-Ir electron transfer, which elevates Ir's d-orbital occupancy, strengthens Ir-C bonds, and weakens C-O bonds. These results confirm that in partially oxidized NiIr nanoclusters, Ir serves as the main center for CO adsorption, while Ni modulates Ir's electronic properties to optimize the balance between adsorption strength and desorption kinetics.

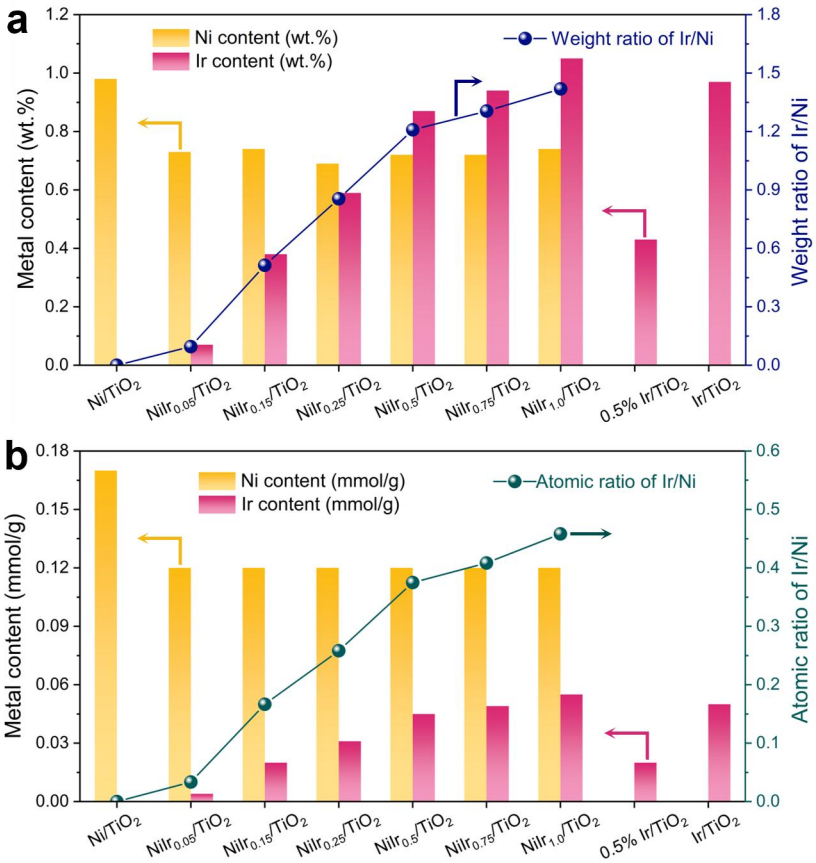

Supplementary Fig. 2. **ICP-AES analysis of metal loadings.** (a) Weight content and (b) atomic content for $NiIr_x/TiO_2$, Ni/TiO_2, and Ir/TiO_2.

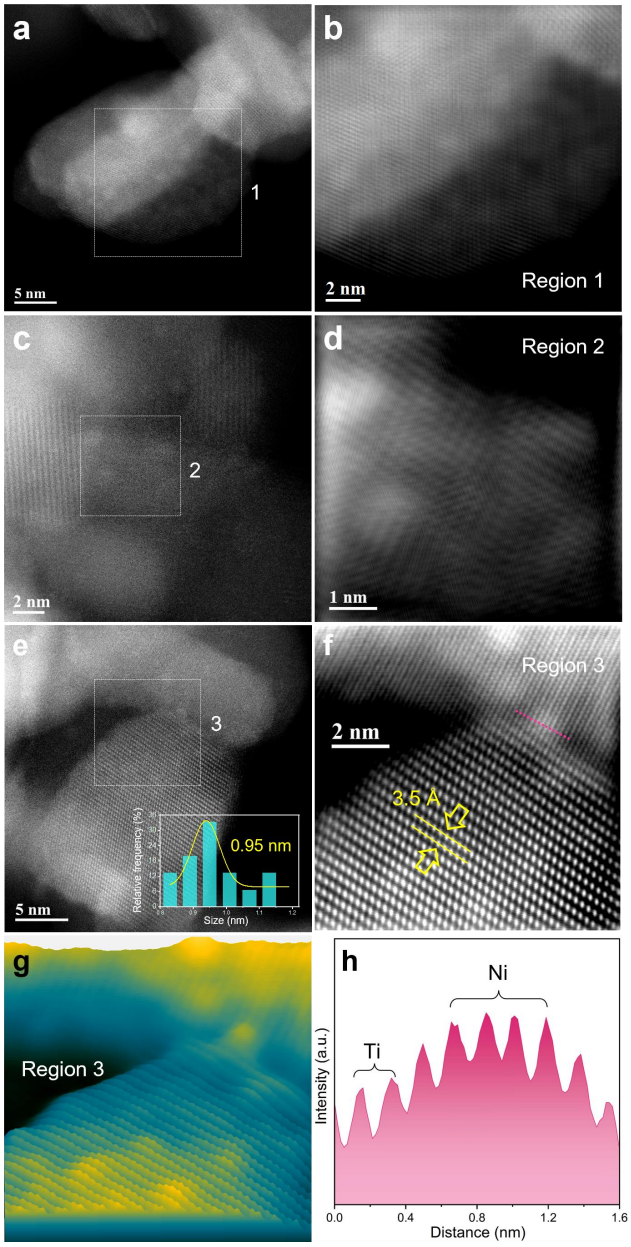

Supplementary Fig. 3. **Monometallic Ni/TiO_2 morphology characterization.** (a, c, and e) Aberration-corrected HAADF-STEM images. Inset in e: Size distribution of Ni nanoclusters. (b, d, and f) Filtered images of regions 1-3 in a, c, and e. (g) 3D surface plot with atomic overlapping of region 3 (Ni: yellow; TiO_2: blue). (h) Intensity profiles along the pink line in f.

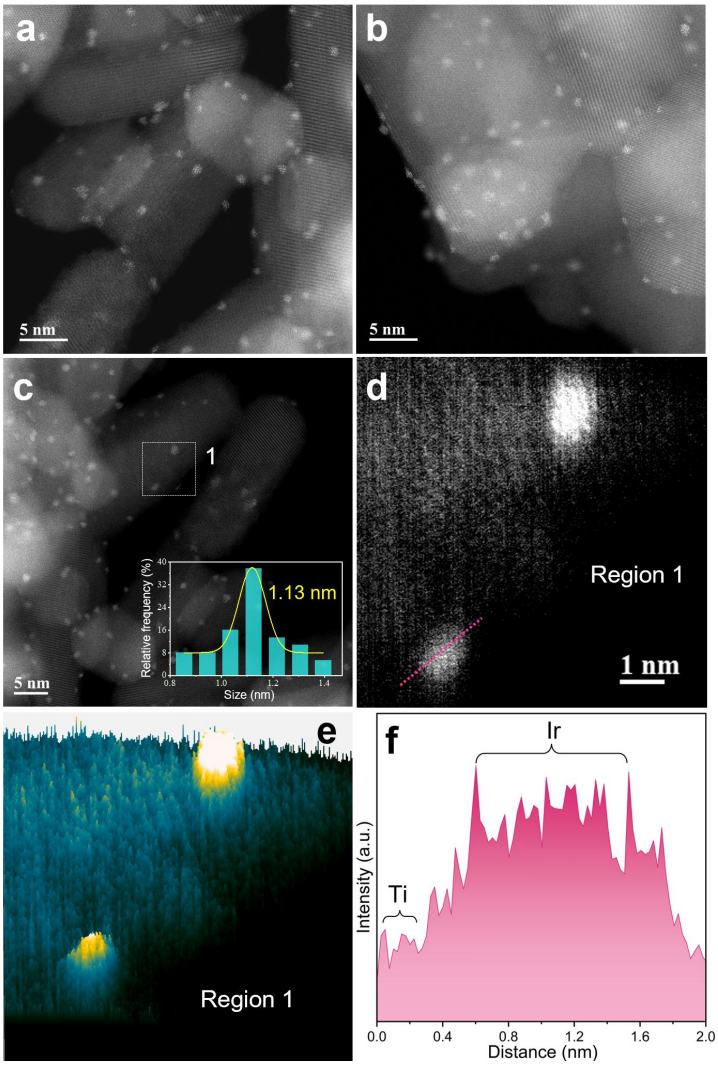

Supplementary Fig. 4. Monometallic Ir/TiO_2 morphology characterization. (a-c) Aberration-corrected HAADF-STEM images. Inset in c: Size distribution of Ir nanoclusters. (d) Filtered atomic image of regions 1 in c. (e) 3D surface plot with atomic overlapping of region 1 (Ir: whitish-yellow; TiO_2: blue). (f) Intensity profiles along the pink line in d.

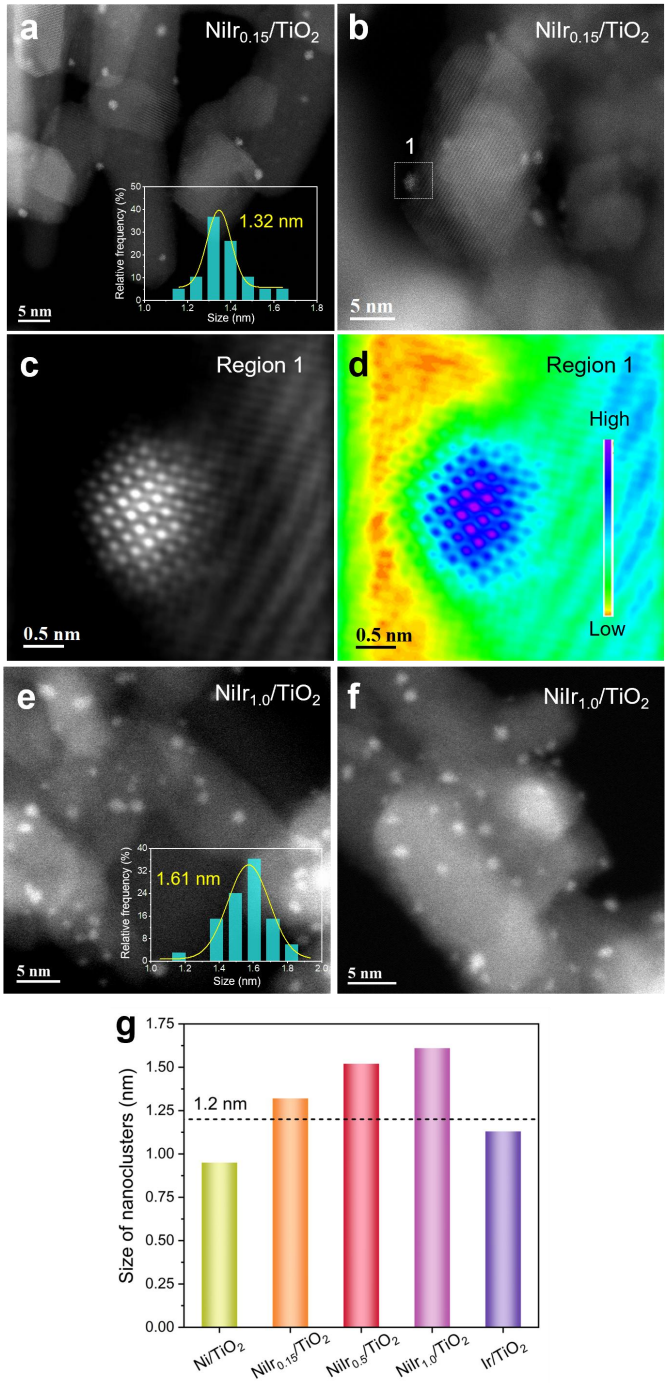

Supplementary Fig. 5. Size evolution of $NiIr_x/TiO_2$ clusters. (a-b) Aberration-corrected HAADF-STEM images of $NiIr_{0.15}/TiO_2$. The size distribution of NiIr nanoclusters is shown in the inset in a. (c) Filtered images of region 1 in b. (d) Color-coded atomic map of region 1 after image filtering. (e-f) HAADF-STEM images of $NiIr_{1.0}/TiO_2$. The size distribution of NiIr nanoclusters is shown in the inset in e. (g) The comparation of the nanocluster size of Ni/TiO_2, Ir/TiO_2, and $NiIr_x/TiO_2$ samples.

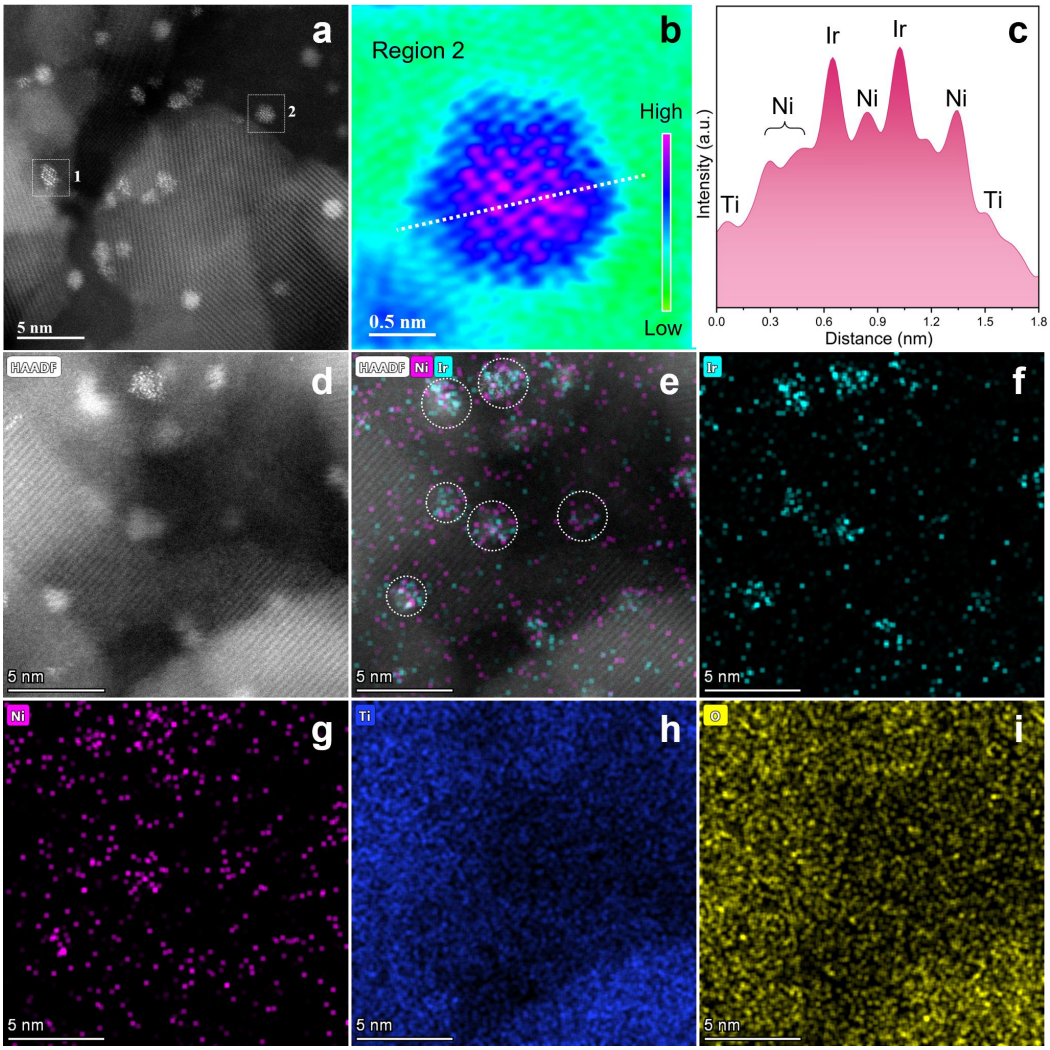

Supplementary Fig. 6. Additional $NiIr_{0.5}/TiO_2$ morphology characterization. (a-b) Aberration-corrected HAADF-STEM image of $NiIr_{0.5}/TiO_2$, and color-coded atomic map of region 2 after image filtering. (c) Intensity profiles along the white line in b. (d-i) HAADF-STEM image and corresponding EDS elemental mapping.

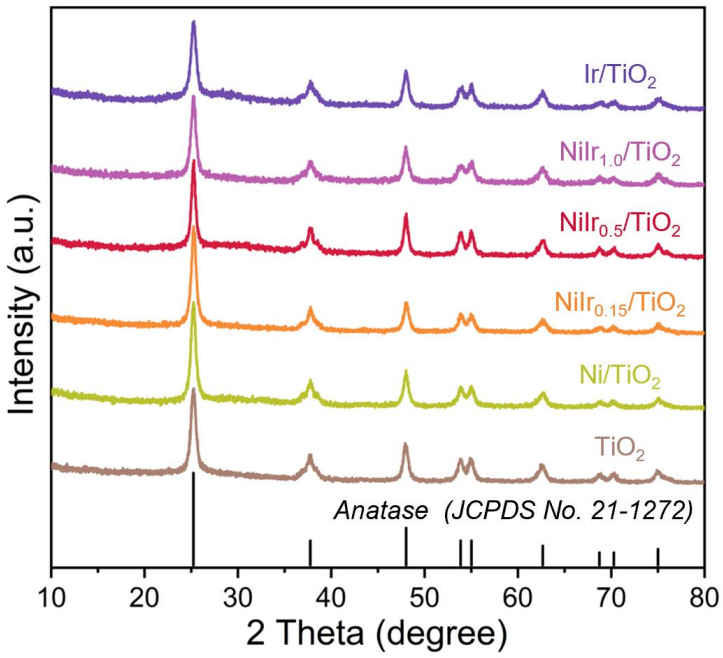

Supplementary Fig. 7. XRD patterns of $NiIr_x/TiO_2$, Ni/TiO_2, and Ir/TiO_2.

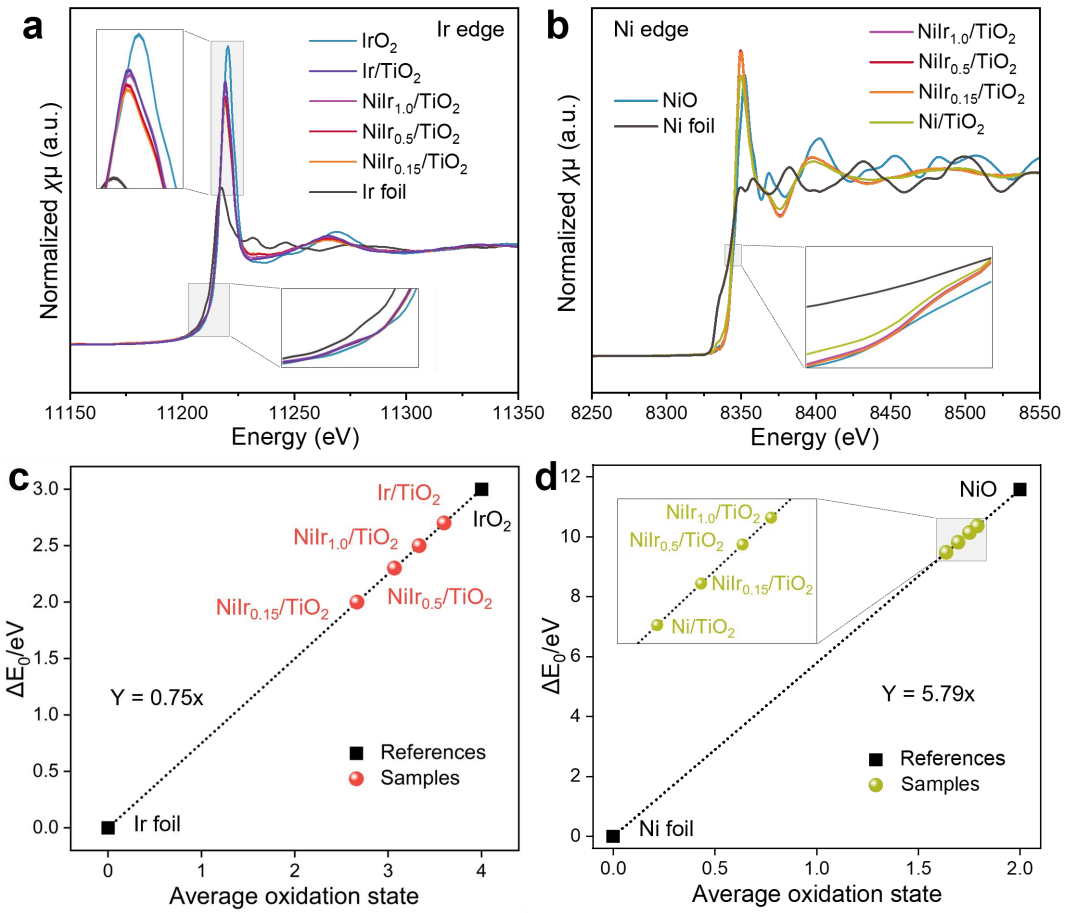

Supplementary Fig. 8. X-ray absorption spectroscopy analysis. (a) Normalized Ir L_3-edge XANES spectra. (b) Normalized Ni K-edge XANES spectra. (c) Linear combination fitting for the position of absorption Ir L_3-edge in XANES curves. (d) Linear combination fitting for the position of absorption Ni K-edge in XANES curves.

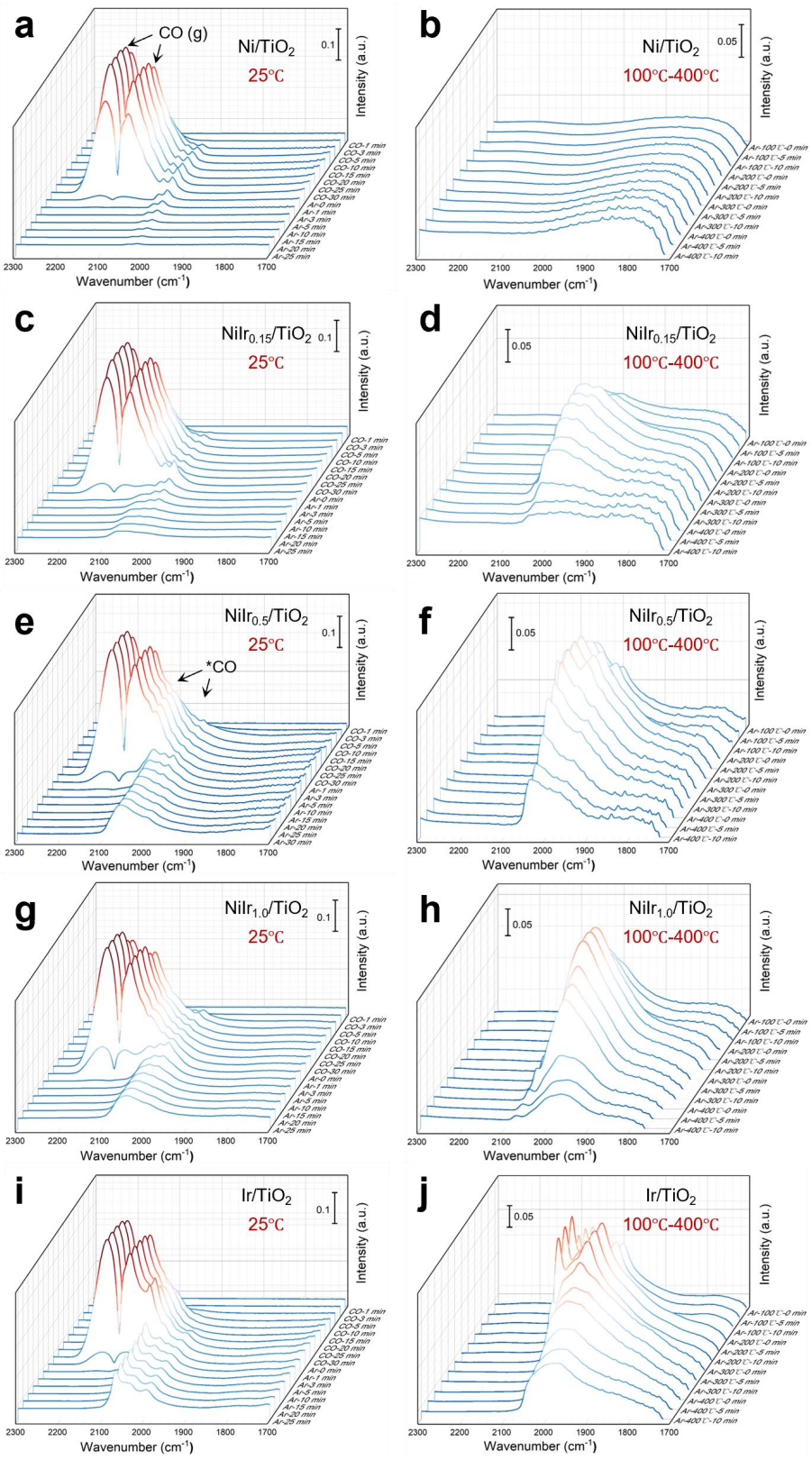

Supplementary Fig. 9. ***In situ*** **CO-probe DRIFTS spectroscopy analysis.** (a-b) Ni/TiO_2. (c-d) $NiIr_{0.15}/TiO_2$. (e-f) $NiIr_{0.15}/TiO_2$. (g-h) $NiIr_{0.15}/TiO_2$. (i-j) $NiIr_{0.15}/TiO_2$. All samples underwent CO adsorption at 25 ℃ for 30 min, followed by Ar-flow desorption at 25 ℃ (30 min) and heating-up desorption up to 400 ℃. Gas-phase CO peaks (2171, 2117 cm^{-1}) were observed during adsorption stage for all samples.

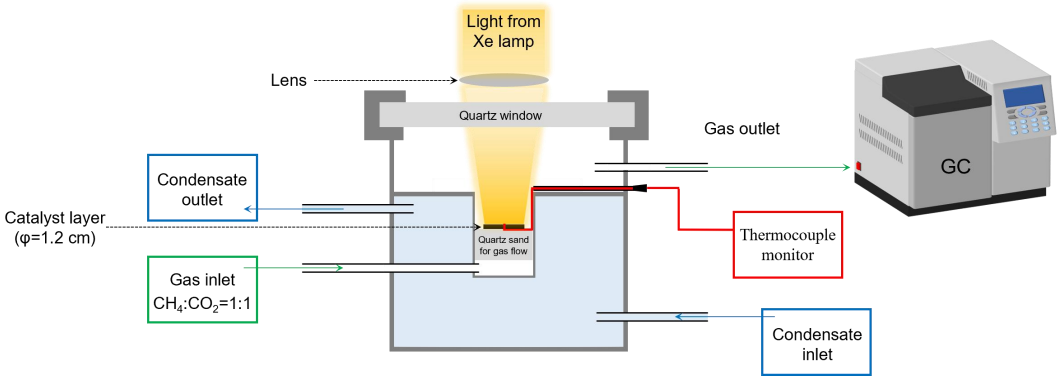

Supplementary Fig. 10. Diagram of the flow reaction setup for light-driven DRM reaction.

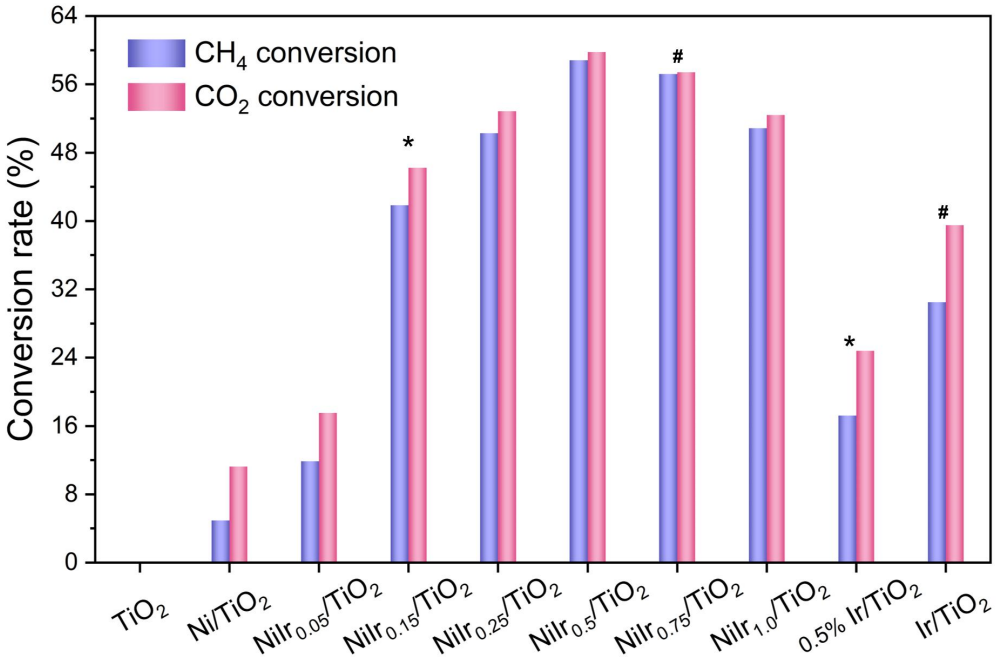

Supplementary Fig. 11. **Conversion rates of TiO_2, Ni/TiO_2, Ir/TiO_2, and $NiIr_x/TiO_2$ under 3.89 W cm^{-2} light irradiation** (feed gas: CH_4:CO_2:Ar =1:1:8). Note: having the same * or # mark indicates that the actual Ir loading amounts of the two sample are similar.

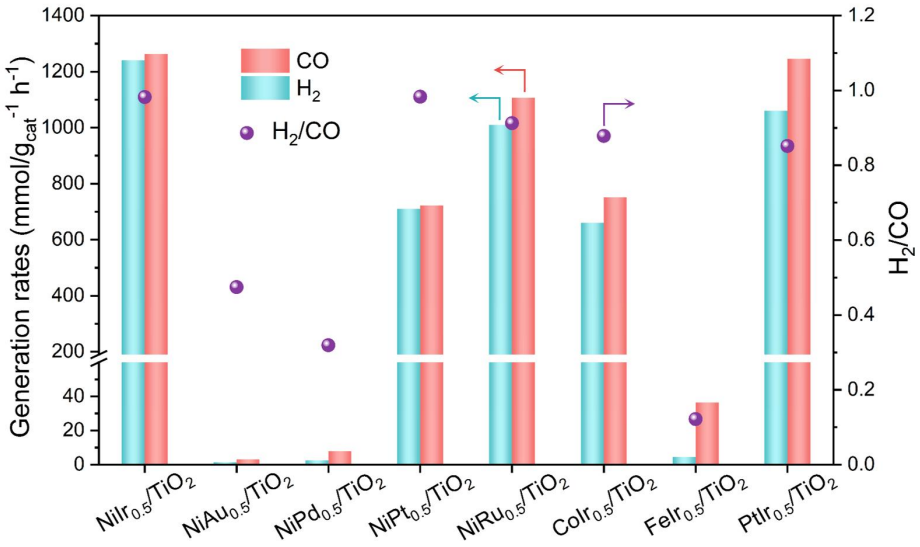

Supplementary Fig. 12. Syngas generation rates and H_2/CO ratios of different bimetal combinations. (3.89 W cm^{-2}, CH_4:CO_2:Ar =1:1:8).

Supplementary Note 2.

For comparative purposes, TiO_2-supported catalysts with various bimetallic combinations were synthesized, maintaining actual metal loadings comparable to that of $NiIr_{0.5}/TiO_2$ (Supplementary Table 1). Among the catalysts, the $NiIr_{0.5}/TiO_2$ catalyst demonstrated superior light-driven DRM performance, exhibiting the highest H_2 and CO production rates with an optimal H_2/CO ratio. Remarkably, its DRM activity surpassed even that of the bimetallic noble metal system $PtIr_{0.5}/TiO_2$.

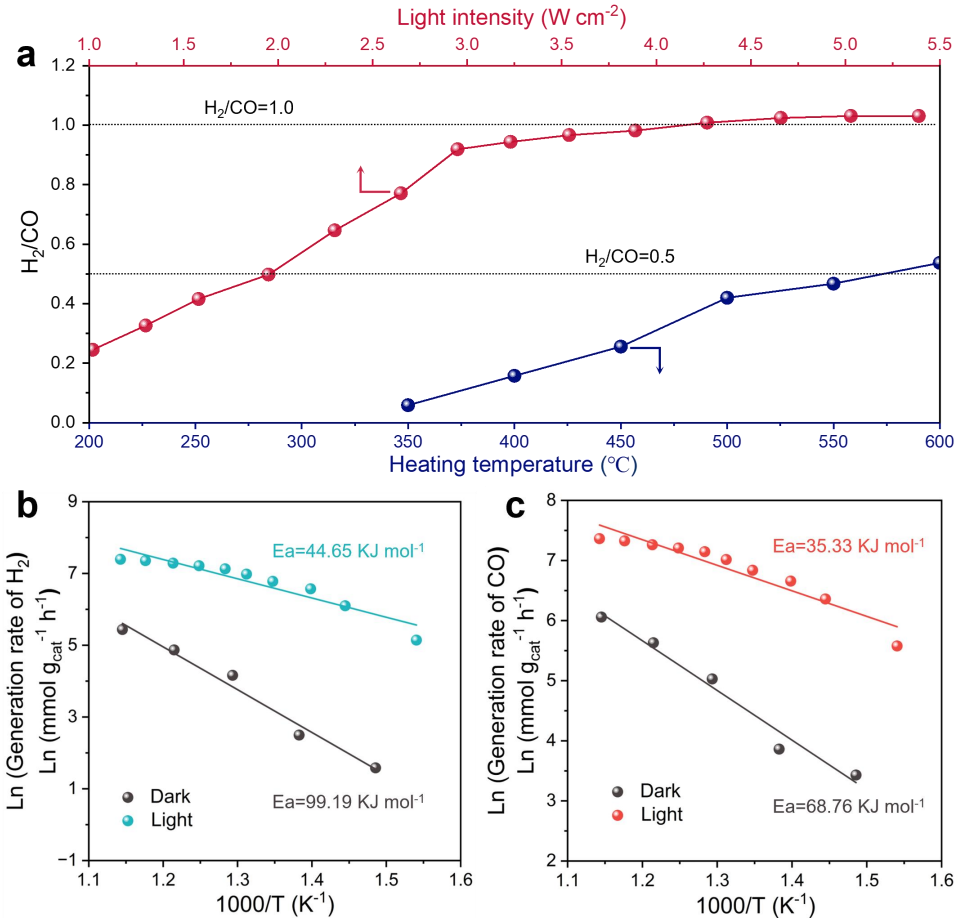

Supplementary Fig. 13. **The influence of light intensity or heating temperature on the H_2/CO ratio, as well as the corresponding Arrhenius plots.** (a) the H_2/CO ratio of $NiIr_{0.5}/TiO_2$ under light irradiation or external heating. (feed gas: CH_4:CO_2:Ar =1:1:8, 5 mg catalyst, flow rate = 20 ml min^{-1}; the heating temperature is near to the detected light irradiation temperature at the center of the catalyst.) The Arrhenius plot in the terms of rate (b) H_2 and (c) CO under light irradiation and external heating conditions. The apparent activation energy (Ea) is calculated by the Arrhenius equation ($k = A\, e^{-Ea/RT}$).

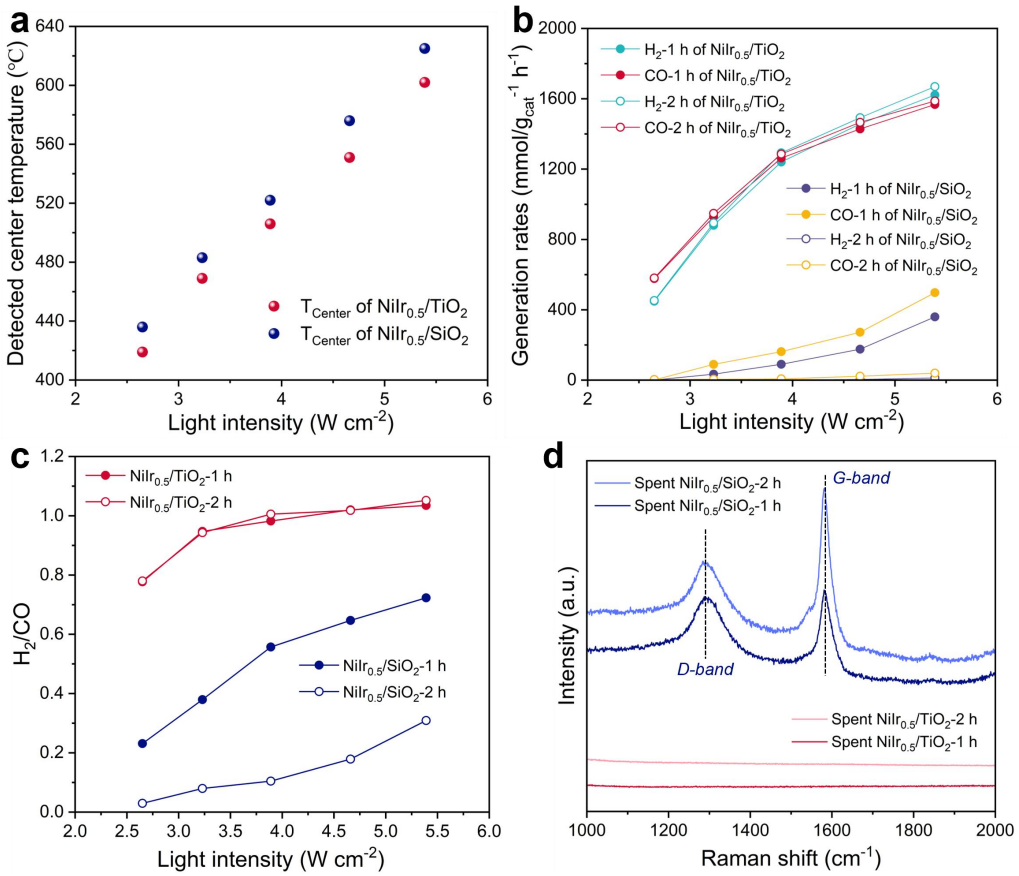

Supplementary Fig. 14. Comparison of light-driven DRM performance and carbon deposition over $NiIr_{0.5}/TiO_2$ and $NiIr_{0.5}/SiO_2$. (a) Detected light irradiation temperature at the center of the catalyst. (b) Syngas generation rates and (c) H_2/CO ratio under different light intensities. (feed gas: CH_4:CO_2:Ar =1:1:8, 5 mg catalyst, flow rate = 20 ml min^{-1}) (d) Raman spectra of spent $NiIr_{0.5}/TiO_2$ and $NiIr_{0.5}/SiO_2$.

Supplementary Note 3.

To further decouple photothermal and photoelectric contributions in light-driven DRM, we compared $NiIr_{0.5}/TiO_2$ and $NiIr_{0.5}/SiO_2$ under identical irradiation. Despite higher surface temperatures on $NiIr_{0.5}/SiO_2$ (Supplementary Fig. 14a), attributed to SiO_2's lower thermal conductivity (1.3-1.4 W m^{-1} K^{-1} vs. TiO_2: 8-10 W m^{-1} K^{-1}), $NiIr_{0.5}/TiO_2$ exhibited superior syngas generation rates and balanced H_2/CO ratios (Supplementary Fig. 14b-c). At 5.39 W cm^{-2}, $NiIr_{0.5}/TiO_2$ achieved CO and H_2 rates of 1567.45 and 1621.81 mmol g_{cat}^{-1} h^{-1} (H_2/CO = 1.06), while $NiIr_{0.5}/SiO_2$ remained below 500 mmol g_{cat}^{-1} h^{-1} (H_2/CO ≤ 0.72). Notably, $NiIr_{0.5}/TiO_2$ maintained stable activity, whereas $NiIr_{0.5}/SiO_2$ showed significant deactivation in 2 hour. Post-reaction Raman spectra (Supplementary Fig. 14d) revealed D-band (1293 cm^{-1}) and intensified G-band (1581 cm^{-1}) signals for $NiIr_{0.5}/SiO_2$ after 2 h, indicating progressive graphitization of carbon deposits. In contrast, $NiIr_{0.5}/TiO_2$ showed negligible carbon accumulation, underscoring the critical role of photoelectric effects in carbon removal. We attribute this divergence to the fact that the photoexcited electron-hole pairs at the NiIr/TiO_2 interface drive non-thermal pathways, which facilitates H-H coupling for H_2 formation and oxidizes carbon intermediates via hole-mediated oxidation, synergizing with photothermal activation. This interfacial synergy is absent in $NiIr_{0.5}/SiO_2$, where purely photothermal heating promotes carbon graphitization and rapid deactivation.

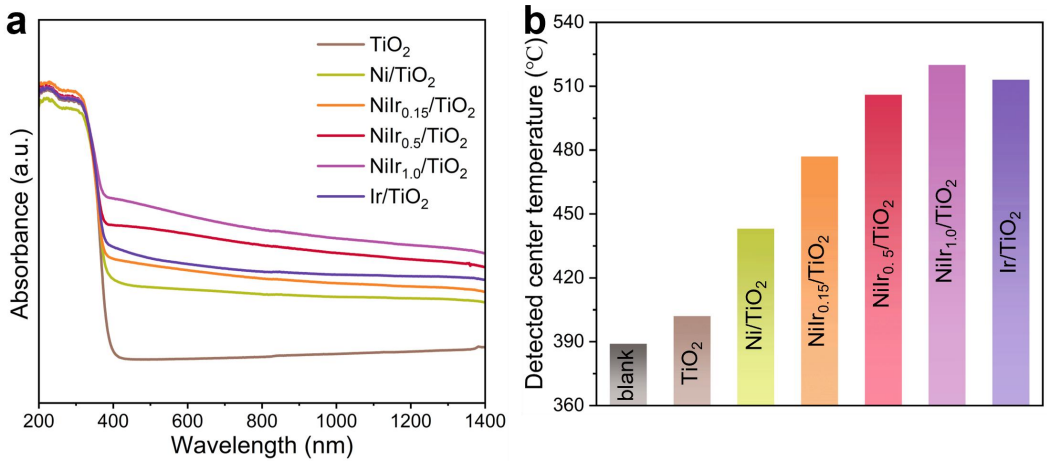

Supplementary Fig. 15. Light absorption capacity of $NiIr_x/TiO_2$, Ni/TiO_2, and Ir/TiO_2. (a) UV-Vis-NIR spectra. (b) Central temperature of catalyst surface under a light intensity of 3.89 Wcm^{-2}.

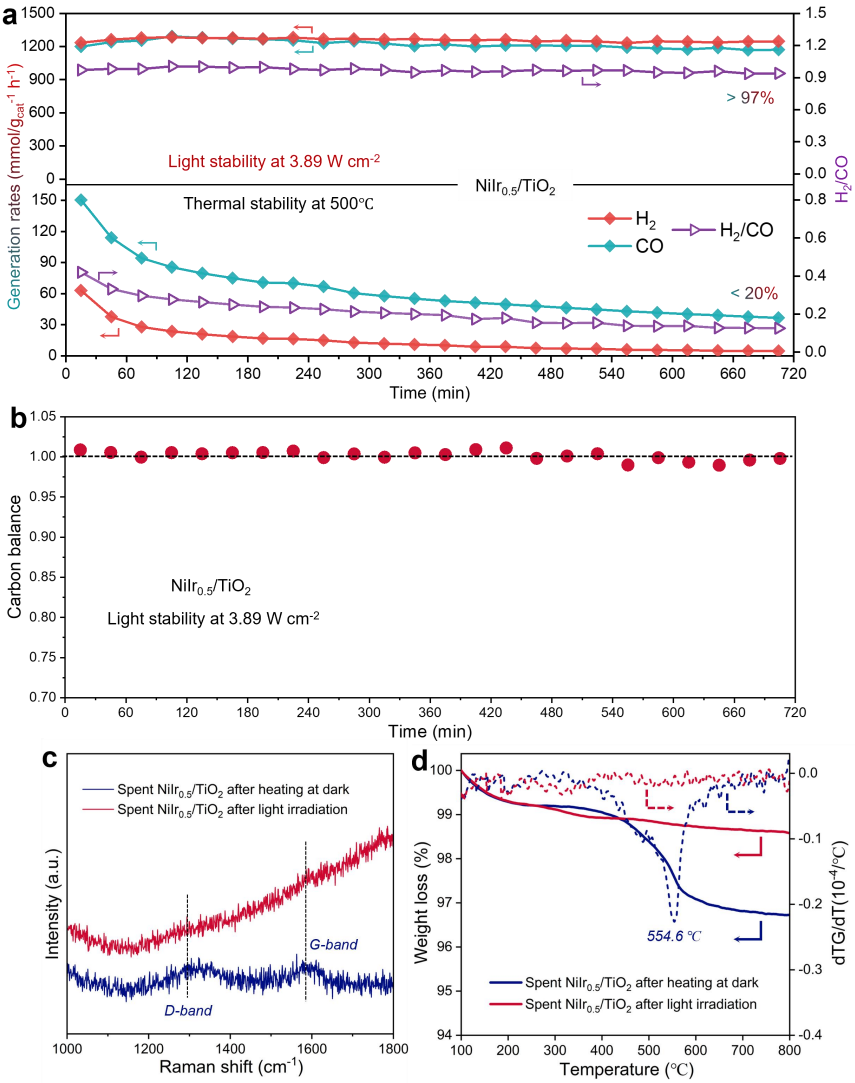

Supplementary Fig. 16. Stability and carbon deposition analysis of NiIr$_{0.5}$/TiO$_2$ under light irradiation or external heating at dark. (a) Long-term catalyst stability of NiIr$_{0.5}$/TiO$_2$ under continuous light irradiation or external heating. (b) Carbon balance under light irradiation during 720 min (CH_4:CO_2:Ar =1:1:8, 5 mg catalyst, flow rate = 20 ml min^{-1}). (c) Raman spectra and (d) Thermogravimetric analysis of NiIr$_{0.5}$/TiO$_2$ after long-time (720 min) light irradiation or heating at dark.

Supplementary Note 4.

Long-term stability tests (Supplementary Fig. 16a-b) demonstrated considerable durability that NiIr$_{0.5}$/TiO$_2$ retained >97% activity over 720 min under light. In contrast, thermal catalysis (heating at 500 °C) suffered a 20% activity drop and significant carbon deposition, emphasizing light's role in suppressing deactivation. Carbon balance is close to unity throughout 720 min test over NiIr$_{0.5}$/TiO$_2$ under light irradiation (Supplementary Fig. 16b). The carbon balance under external heating at dark was not calculated due to the very low conversion (<8%) for reliability purposes. Raman spectra (Supplementary Fig. 16c) of NiIr$_{0.5}$/TiO$_2$ after heating at dark showed typical D-band and G-band of carbonaceous species Thermogravimetric analysis verified the severe carbon deposition especially at 554.6 ℃ of NiIr$_{0.5}$/TiO$_2$ after heating at dark (Supplementary Fig. 16d).

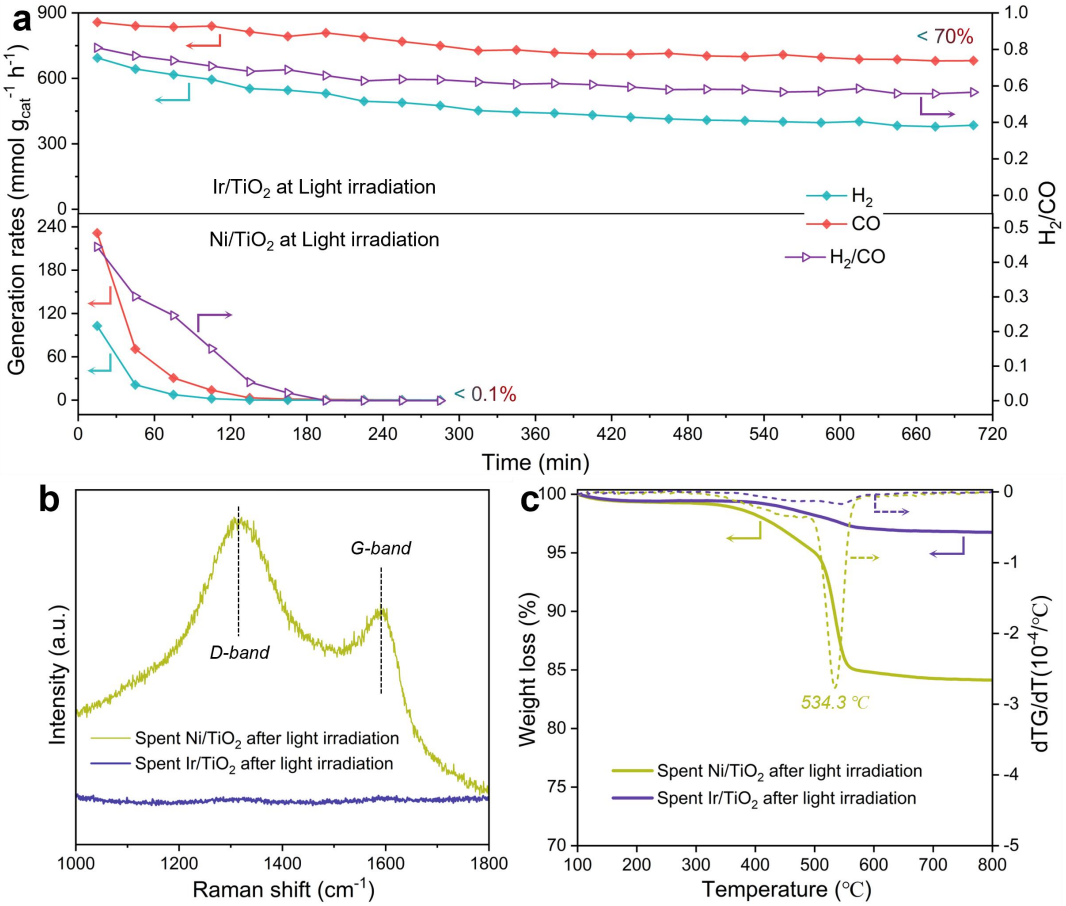

Supplementary Fig. 17. Stability test of Ni/TiO$_2$ and Ir/TiO$_2$ and carbon deposition analysis. (a) Long-term catalyst stability of Ni/TiO$_2$ and Ir/TiO$_2$ under continuous light irradiation (feed gas: CH$_4$:CO$_2$:Ar =1:1:8, 5 mg catalyst, flow rate = 20 ml min^{-1}). (b) Raman spectra and (c) Thermogravimetric analysis of Ni/TiO$_2$ and Ir/TiO$_2$ after long-time light irradiation.

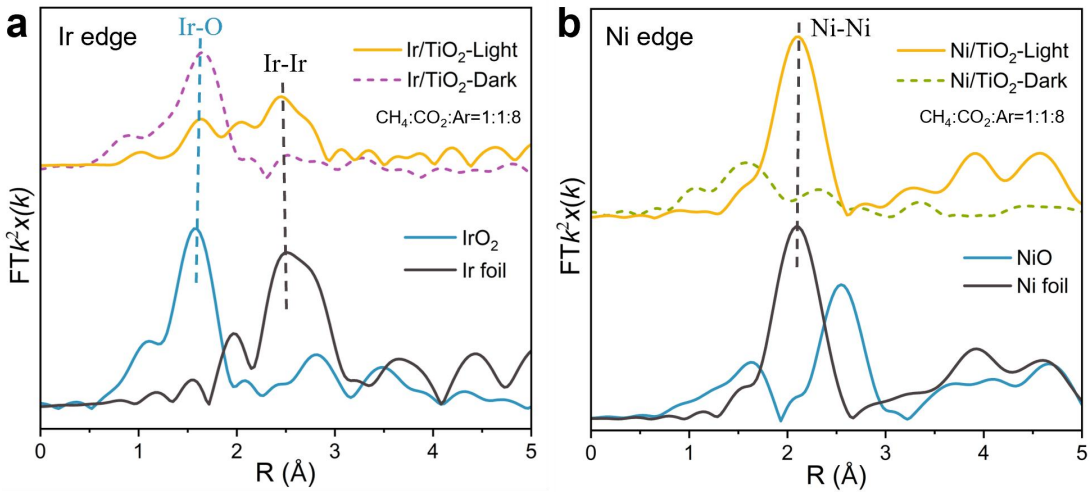

Supplementary Fig. 18. *In situ* XAS analysis of monometallic-loaded TiO_2 samples during light-driven DRM conditions. (a) *In situ* k^2-weighted Fourier transform of Ir L_3-edge EXAFS spectra for Ir/TiO_2. (b) *In situ* k^2-weighted Fourier transform of Ni K-edge EXAFS spectra for Ni/TiO_2. Data are not phase-corrected. Conditions: CH_4:CO_2:Ar =1:1:8, 3.89 W cm^{-2}.

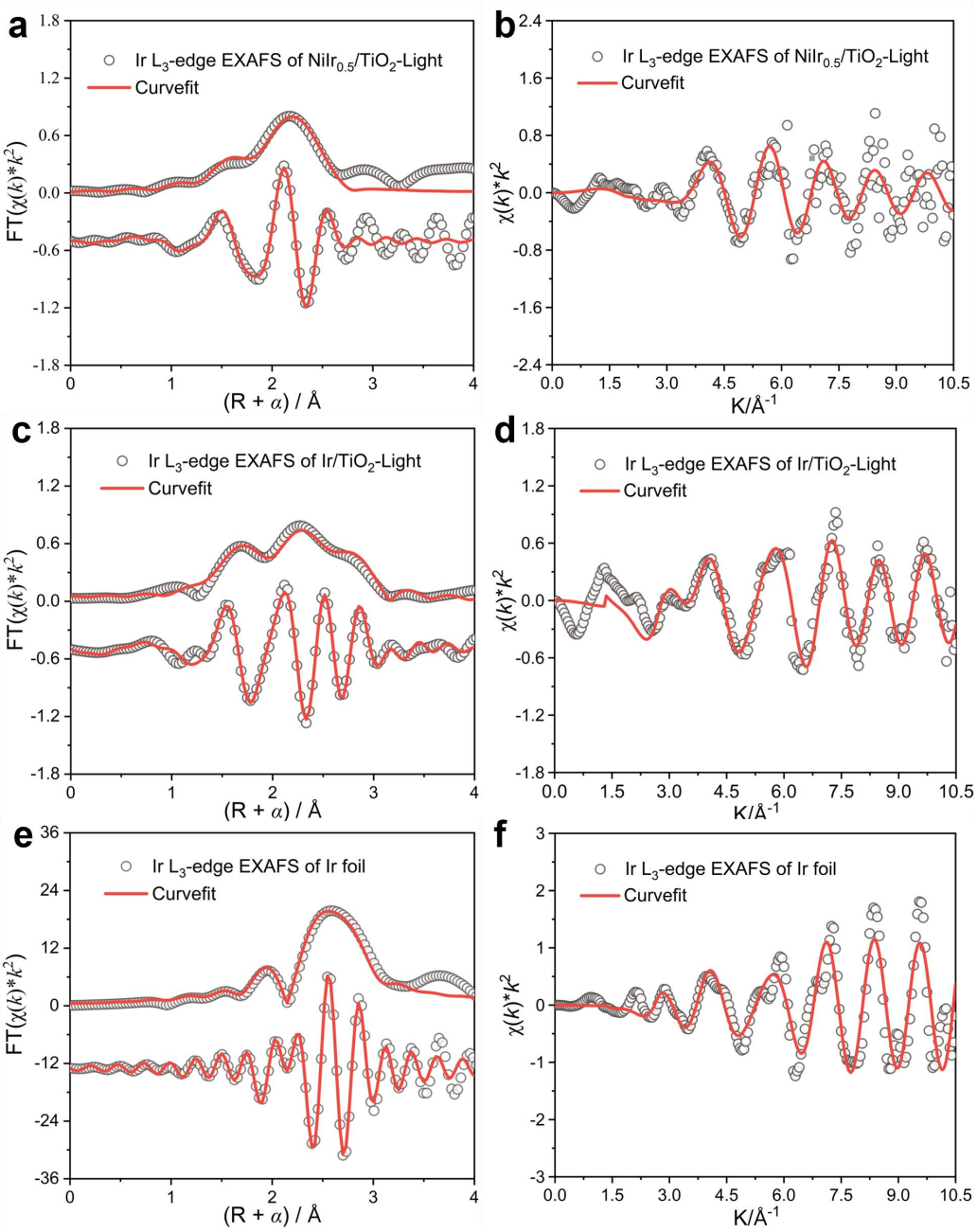

Supplementary Fig. 19. Ir L_3-edge EXAFS (circles) and curvefit (line) shown in R-space and k^2-weighted K-space. EXAFS fitting of (a-b) $NiIr_{0.5}/TiO_2$ and (c-d) Ir/TiO_2 during light-driven DRM conditions. (e-f) EXAFS fitting of Ir foil. Data are k^2-weight and not phase-corrected.

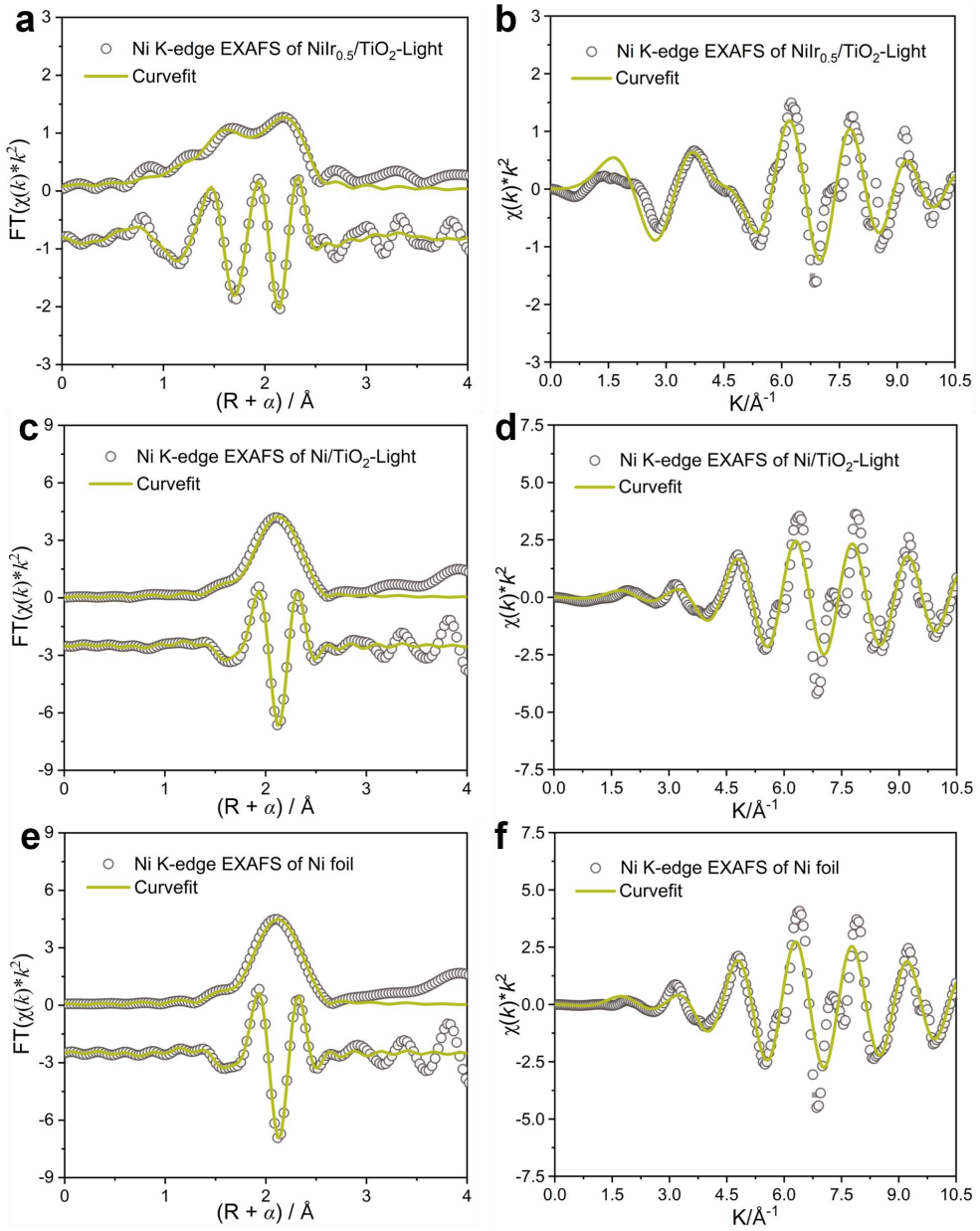

Supplementary Fig. 20. Ni K-edge EXAFS (circles) and curvefit (line) shown in R-space and k^2-weighted K-space. EXAFS fitting of (a-b) $NiIr_{0.5}/TiO_2$ and (c-d) Ni/TiO_2 during light-driven DRM conditions. (e-f) EXAFS fitting of Ni foil. Data are k^2-weight and not phase-corrected.

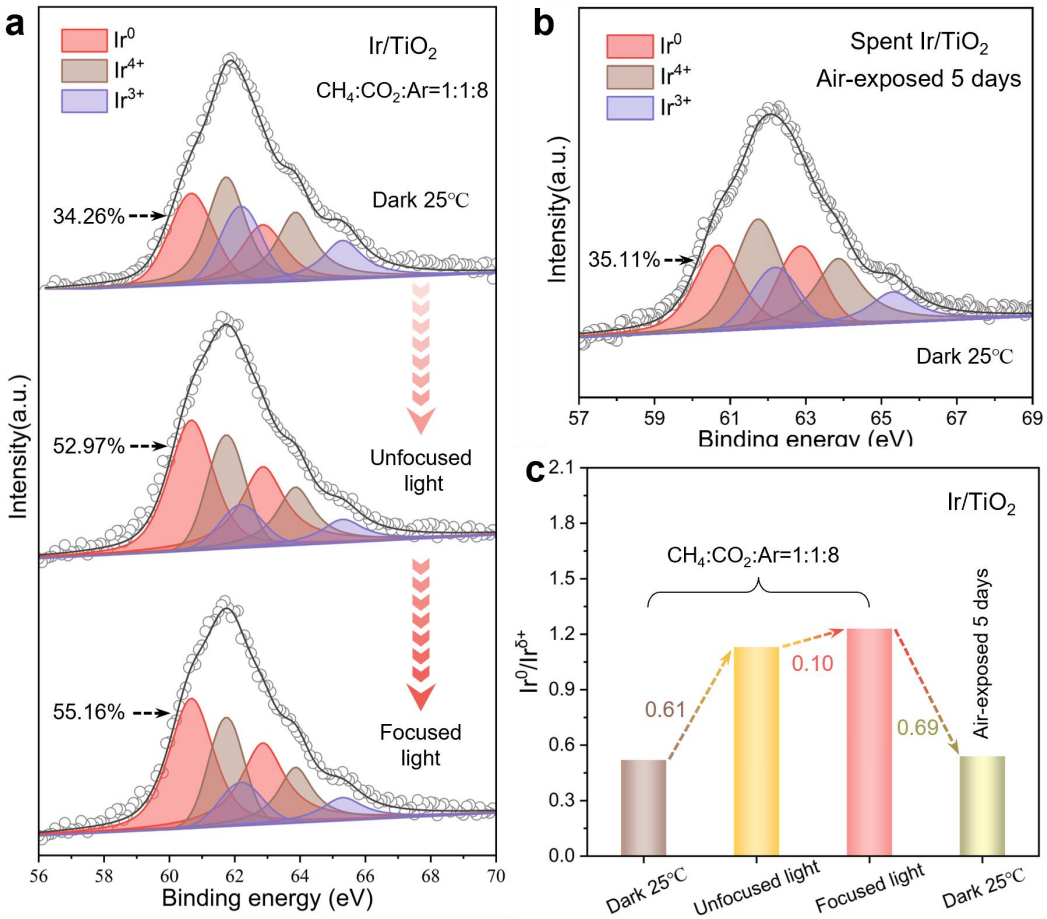

Supplementary Fig. 21. NAP-XPS analysis of Ir/TiO_2. (a) *In situ* NAP-XPS spectra of Ir 4f for Ir/TiO_2 under different irradiation conditions in a gas flow of CH_4:CO_2:Ar =1:1:8 (Unfocused light: 1.58 W cm^{-2}; focused light: 3.89 W cm^{-2}). (b) XPS spectra of Ir 4f for spent Ir/TiO_2 exposed in air for 5 days. (c) $Ir^0/Ir^{\delta+}$ ratio evolution of Ir/TiO_2 during *in situ* NAP-XPS conditions and post-air exposure, derived from deconvolution of the XPS spectra.

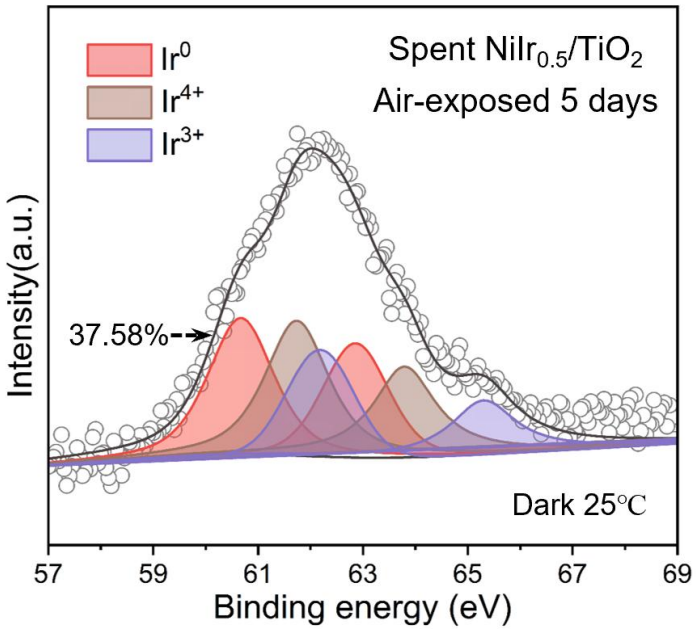

Supplementary Fig. 22. XPS spectra of Ir 4f for spent $NiIr_{0.5}/TiO_2$ exposed in air for 5 days.

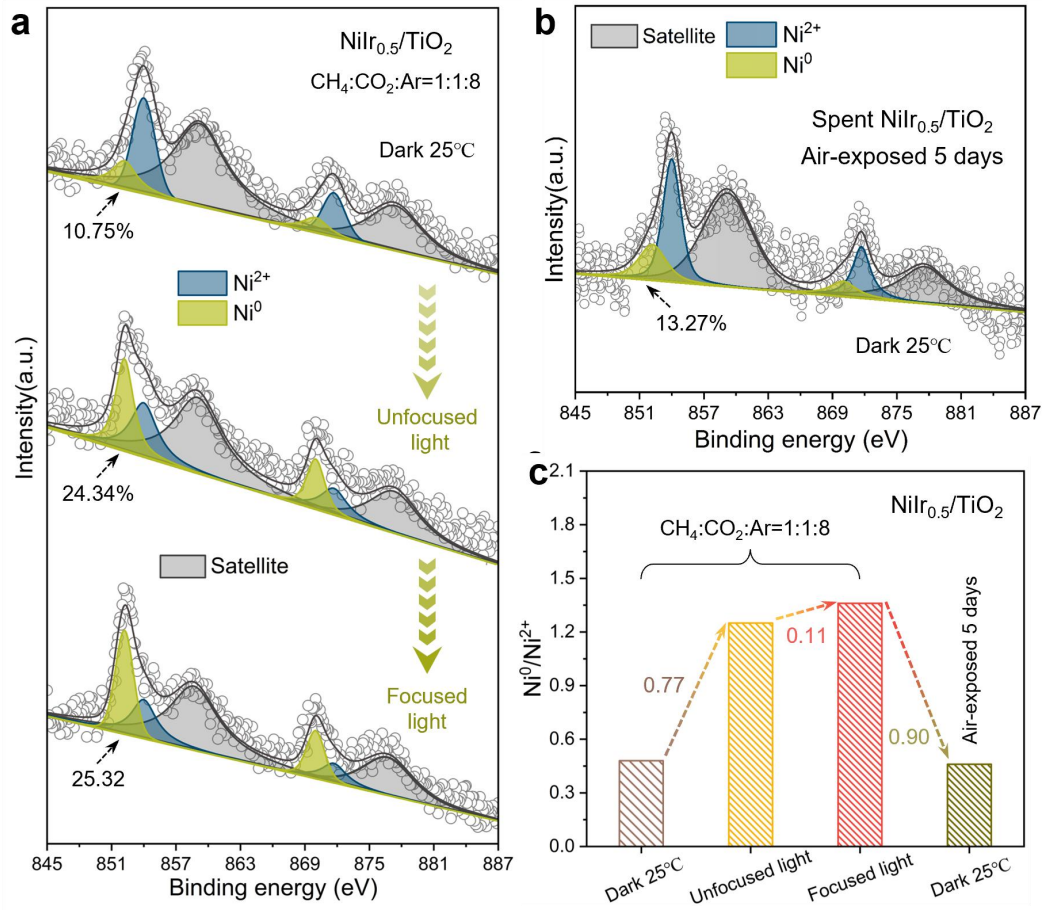

Supplementary Fig. 23. NAP-XPS analysis of Ni 2p for $NiIr_{0.5}/TiO_2$. (a) *In situ* NAP-XPS spectra under different irradiation conditions in a gas flow of CH_4:CO_2:Ar =1:1:8 (Unfocused light: 1.58 W cm^{-2}; focused light: 3.89 W cm^{-2}). (b) XPS spectra of Ni 2p for spent $NiIr_{0.5}/TiO_2$ exposed in air for 5 days. (c) Ni^0/Ni^{2+} ratio evolution of $NiIr_{0.5}/TiO_2$ during *in situ* NAP-XPS conditions and post-air exposure, derived from deconvolution of the XPS spectra.

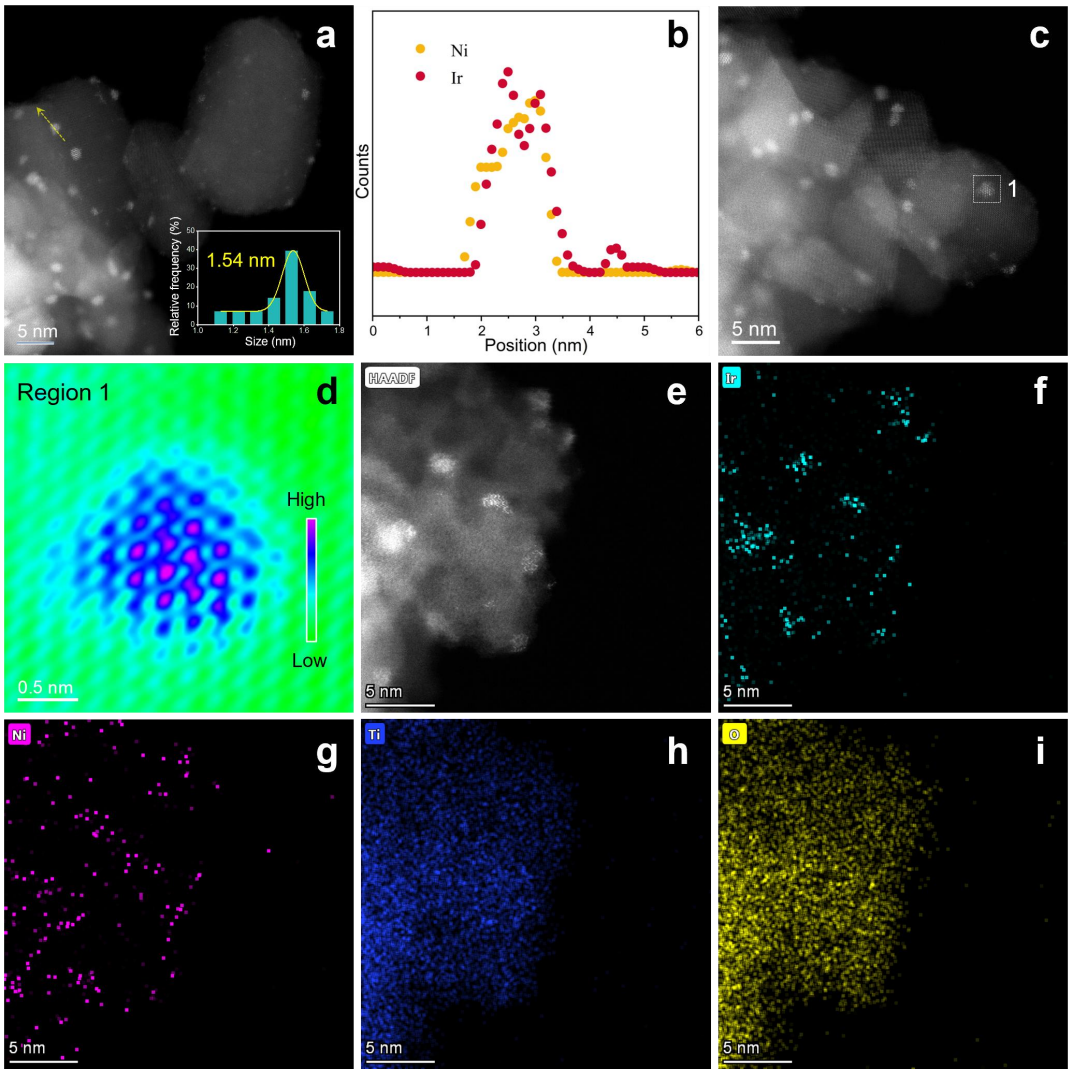

Supplementary Fig. 24. Spent $NiIr_{0.5}/TiO_2$ morphology characterization. (a) Aberration-corrected HAADF-STEM image of spent $NiIr_{0.5}/TiO_2$ and cluster size distribution (inset). (b) EDS line-scan profiles of Ni and Ir across a cluster along the yellow arrow in **a**. (c-d) Aberration-corrected HAADF-STEM image, and color-coded atomic map of region 1 after image filtering. (e-i) HAADF-STEM image and corresponding EDS elemental mapping.

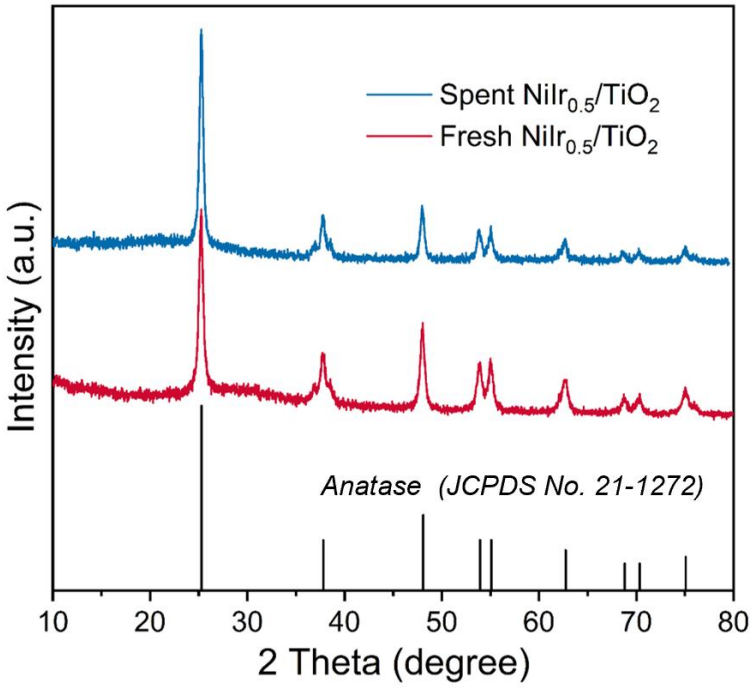

Supplementary Fig. 25. XRD patterns of $NiIr_{0.5}/TiO_2$ before and after 12 h light-driven DRM reaction.

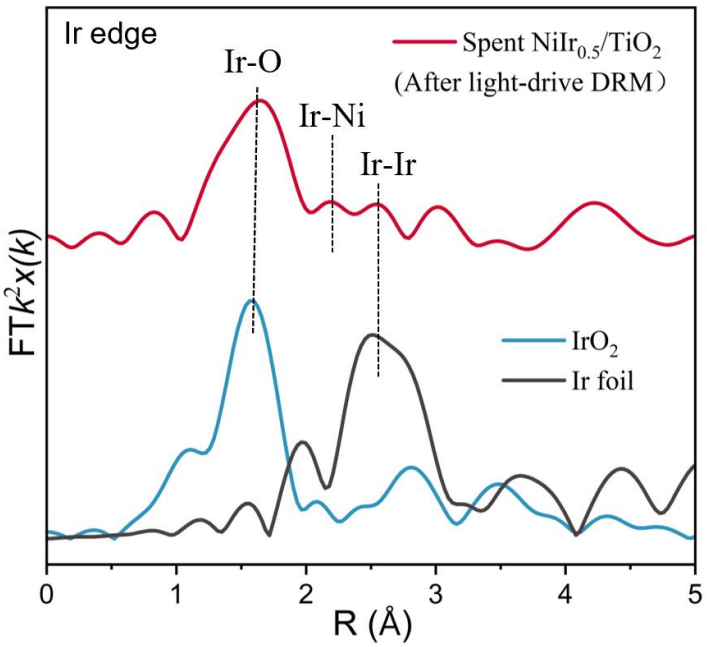

Supplementary Fig. 26. k^2-weighted Fourier transform of Ir L_3-edge EXAFS spectra for $NiIr_{0.5}/TiO_2$ after 12 h light-driven DRM reaction.
(Data are not phase-corrected.)

Supplementary Note 5.

Compared to the pre-reaction state, the NiIr nanoclusters after prolonged light-driven DRM exhibit a slight increase in average size, from 1.52 nm to 1.54 nm (Supplementary Fig. 24). EDS line scans, filtered and color-coded HAADF-STEM images, and elemental mapping confirm that Ni and Ir atoms retain intimate contact. Post-reaction XRD patterns show only the characteristic anatase TiO_2 peaks, with no additional reflections from metallic phases, verifying that the NiIr nanoclusters remain dispersed on the TiO_2 support (Supplementary Fig. 25). The k^2-weighted Fourier transform of Ir L_3-edge EXAFS spectra for $NiIr_{0.5}/TiO_2$ after 12 h of reaction further reveals partial re-oxidation of the clusters (Supplementary Fig. 26), consistent with the NAP-XPS observations of air-exposed samples regaining their initial oxidized state. These results confirm that the NiIr nano-island alloy forms exclusively during light-driven DRM and gradually re-oxidizes to its initial state after light cessation.

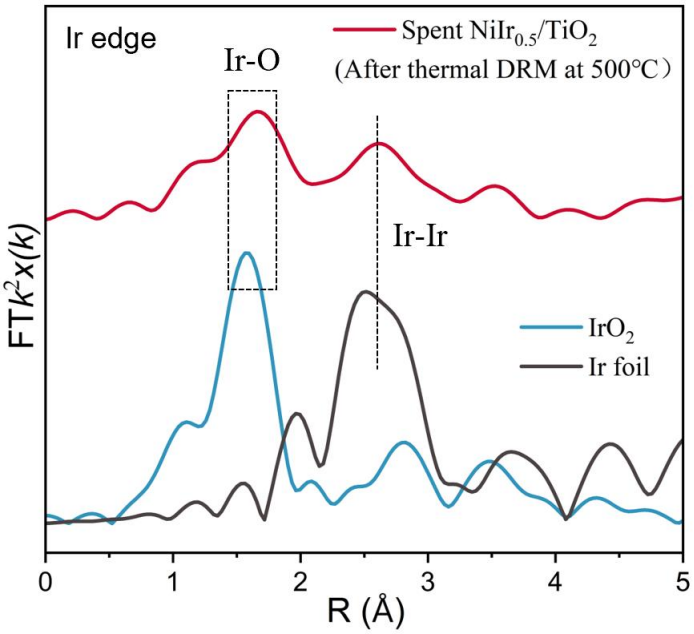

Supplementary Fig. 27. k^2-weighted Fourier transform of Ir L_3-edge EXAFS spectra for $NiIr_{0.5}/TiO_2$ after 12 h thermal DRM reaction at 500 °C.

(Data are not phase-corrected.)

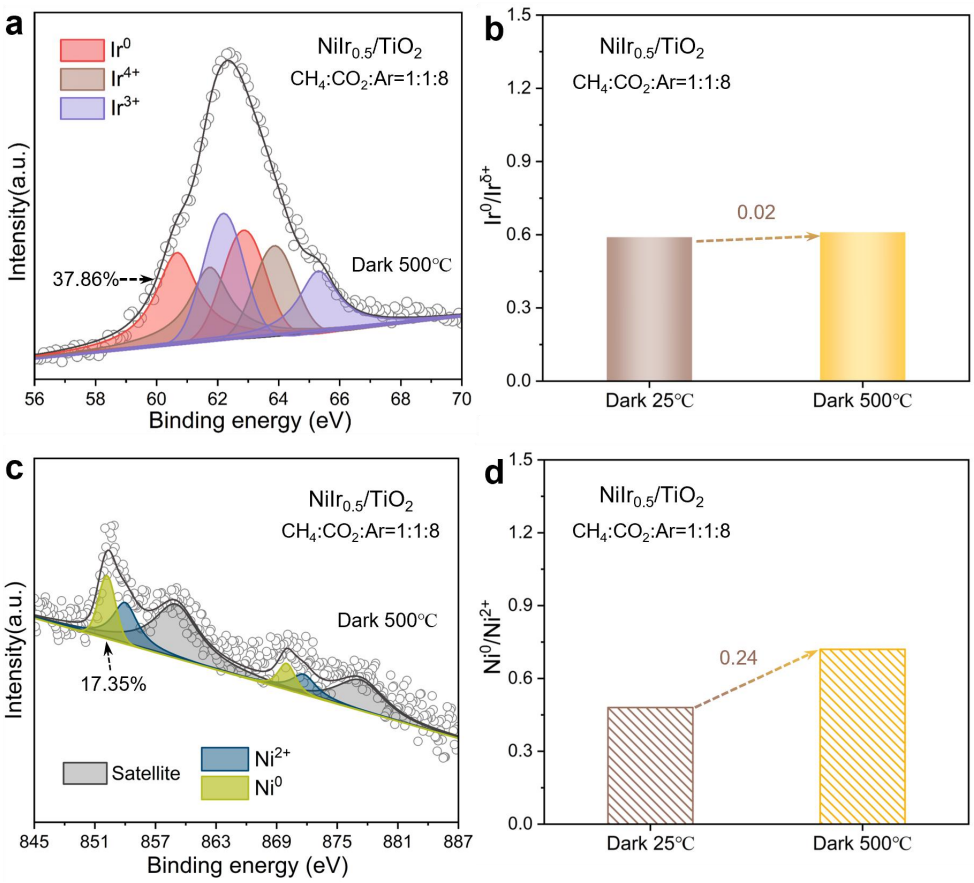

Supplementary Fig. 28. *In situ* NAP-XPS analysis of $NiIr_{0.5}/TiO_2$ under thermal DRM in the dark. (a) Ir 4f spectra during reaction at 500 °C, and (b) corresponding $Ir^0/Ir^{\delta+}$ ratio evolution in a gas flow of CH_4:CO_2:Ar =1:1:8. (c) Ni 2p spectra during reaction at 500 °C, and (b) corresponding Ni^0/Ni^{2+} ratio evolution in a gas flow of CH_4:CO_2:Ar =1:1:8.

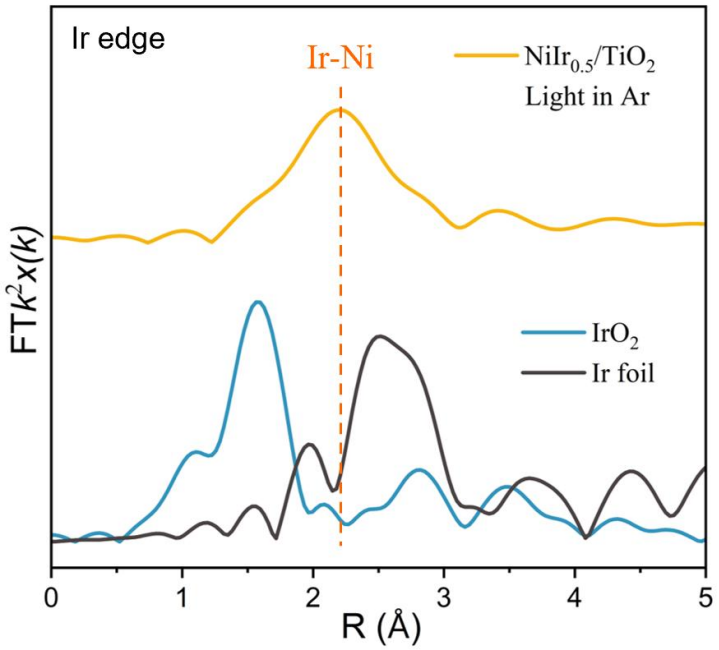

Supplementary Fig. 29. *In situ* k^2-weighted Fourier transform of Ir L_3-edge EXAFS spectra for $NiIr_{0.5}/TiO_2$ under light in Argon.
(Data are not phase-corrected.)

Supplementary Note 6.

To exclude potential influences of CH_4 and CO_2 on NiIr alloy formation, supplementary *in situ* experiments were conducted under argon atmosphere. Notably, light irradiation in Ar still induces a distinct Ni-Ir scattering peak at 2.18 Å in the Ir L_3-edge EXAFS spectra (Supplementary Fig. 29), confirming that reactant gases are dispensable for alloy formation. *In situ* NAP-XPS in Ar (Supplementary Fig. 30) demonstrates that unfocused light reduces both Ir and Ni, elevating the $Ir^0/Ir^{\delta+}$ and Ni^0/Ni^{2+} ratios by 1.03 and 0.72, respectively, compared to the initial dark conditions. Focused light further elevates these ratios by 0.26 (Ir) and 0.04 (Ni), demonstrating intensity-dependent reduction. Upon immediate light cessation in Ar, rapid re-oxidation of Ni and Ir occurs, though not fully reverting to the pre-reaction state. This partial recovery underscores the dynamic reversibility of the photoinduced NiIr nano-island alloy, which fully regenerates to the initial Ox-$NiIr/TiO_2$ configuration after prolonged air exposure.

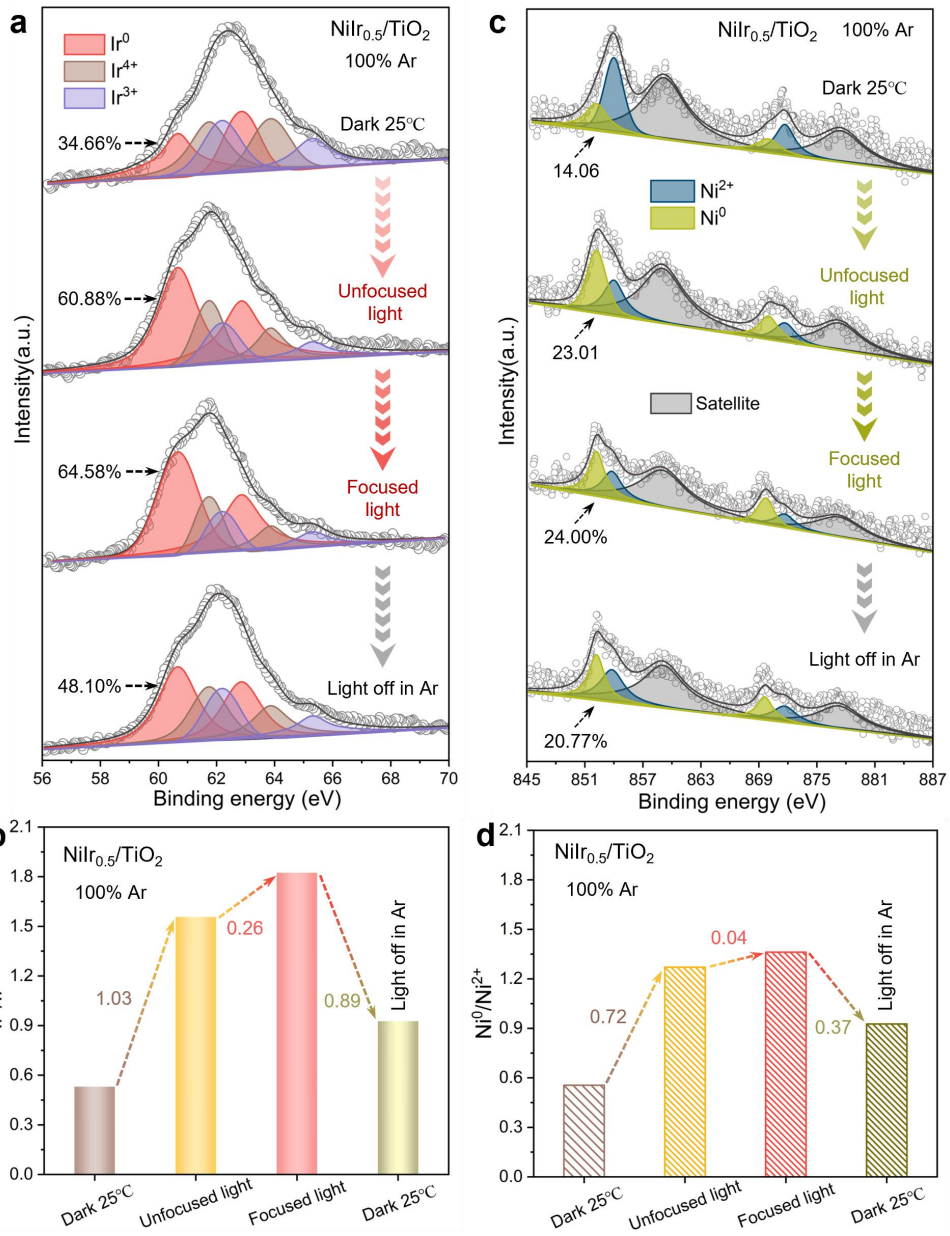

Supplementary Fig. 30. *In situ* NAP-XPS spectra for $NiIr_{0.5}/TiO_2$ under different irradiation conditions in 100% argon atmosphere. (a) Ir 4f spectra and (b) corresponding $Ir^0/Ir^{\delta+}$ ratio evolution. (c) Ni 2p spectra and (d) corresponding Ni^0/Ni^{2+} ratio evolution.

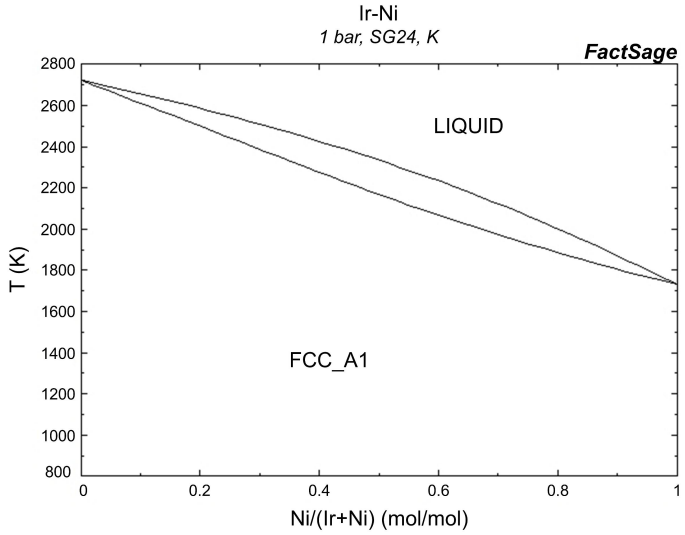

Supplementary Fig. 31. The binary phase diagram of Ir-Ni.
(https://www.crct.polymtl.ca/FACT/documentation/#opennewwindow)

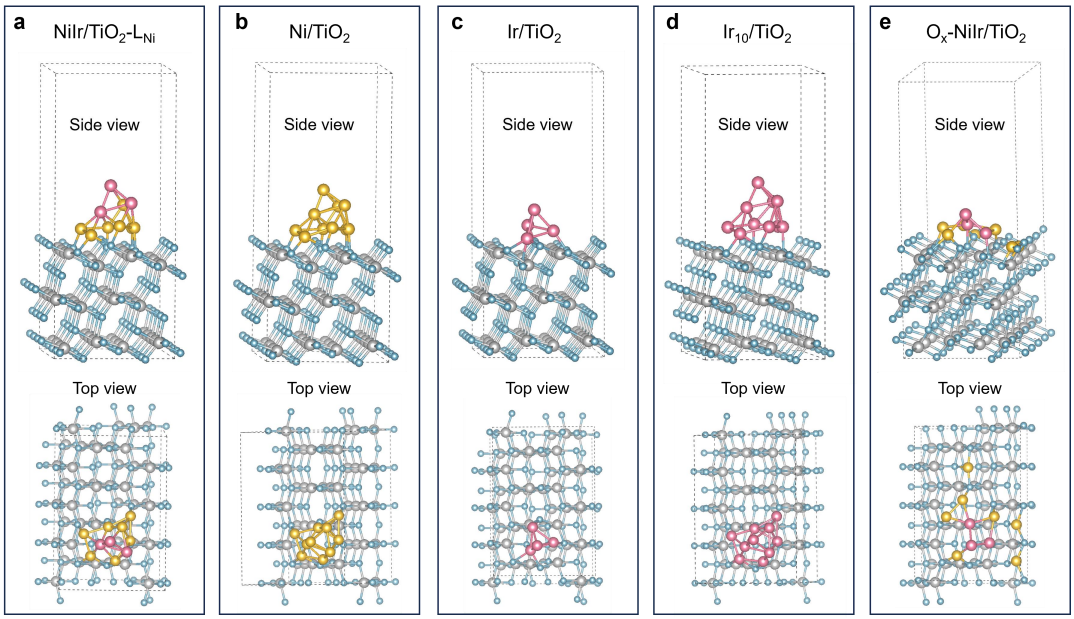

Supplementary Fig. 32. DFT-optimized structures. (a) $NiIr/TiO_2$-L_{Ni} model formed under photoexcitation. (b) Ni/ TiO_2 model formed under photoexcitation. (c) Ir/TiO_2 model formed under photoexcitation. (d) Ir_{10}/TiO_2 model for property comparison. (e) O_x-$NiIr/TiO_2$ model before photoirradiation or under thermal catalysis. Ir, Ni, Ti, and O atoms are shown in pink, yellow, grey, and blue colors, respectively.

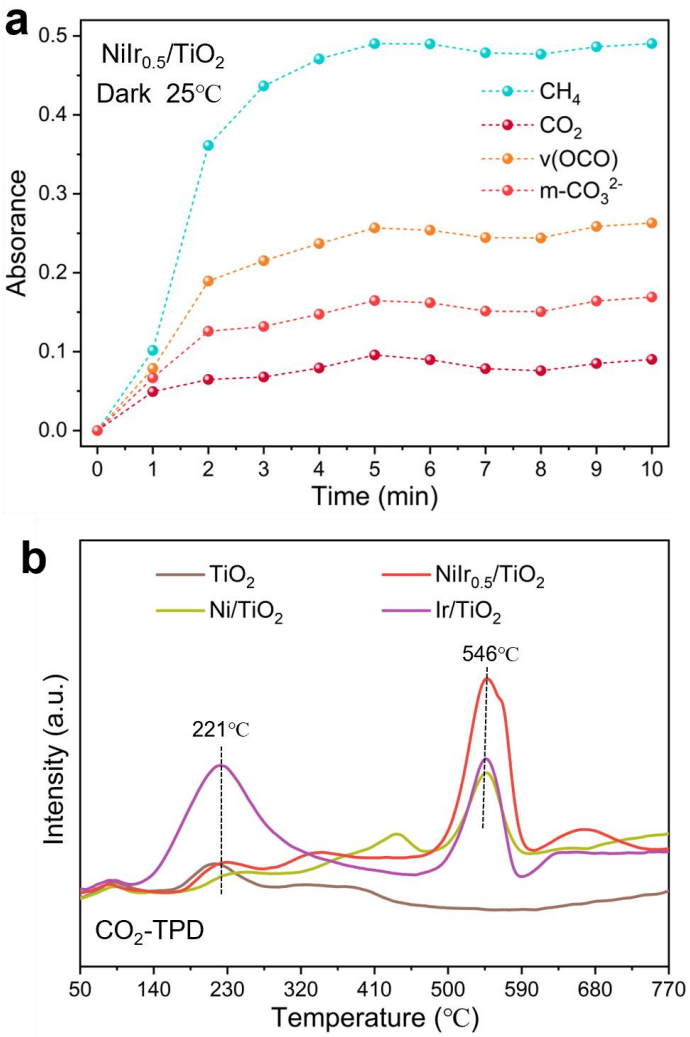

Supplementary Fig. 33. Reactant gas adsorption analysis on NiIr/TiO_2 in the dark. (a) Time-resolved evolution of dominant SR-DRIFTS peaks during CO_2-CH_4 co-adsorption in the dark (25 ℃, CH_4:CO_2:Ar =1:1:8). (b) CO_2-TPD profiles of TiO_2, Ni/TiO_2, $NiIr_{0.5}/TiO_2$, and Ir/TiO_2.

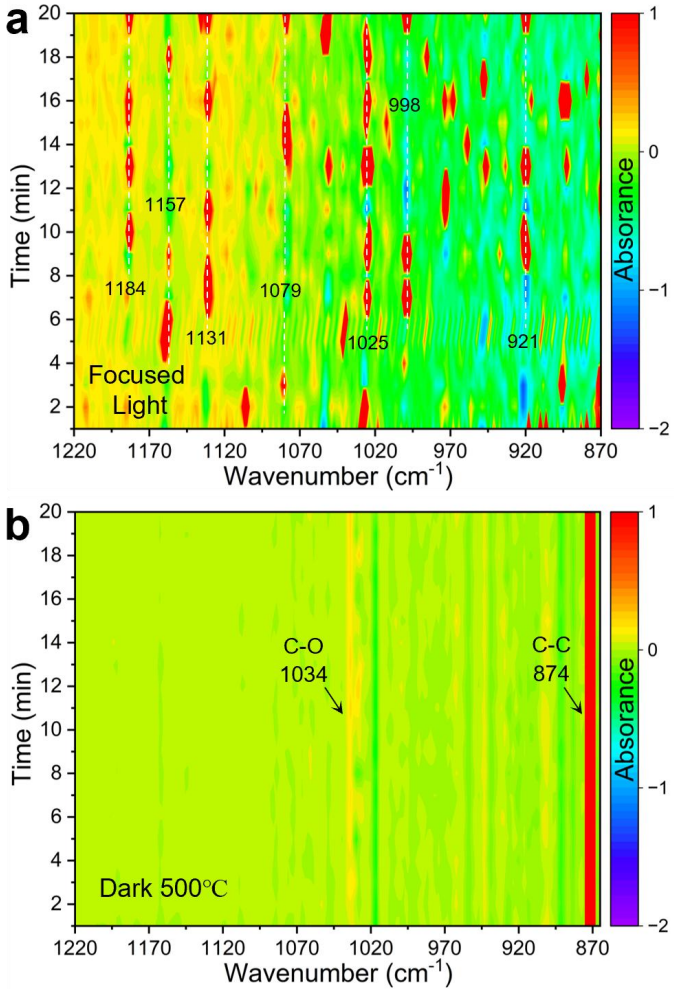

Supplementary Fig. 34. *In-situ* SR-DRIFTS (<1220 cm^{-1}) of $NiIr_{0.5}/TiO_2$ in a gas flow of CH_4:CO_2:Ar =1:1:8. (a) Under 3.89 W cm^{-2} focused light. (b) Under 500 ℃ heating in the dark.

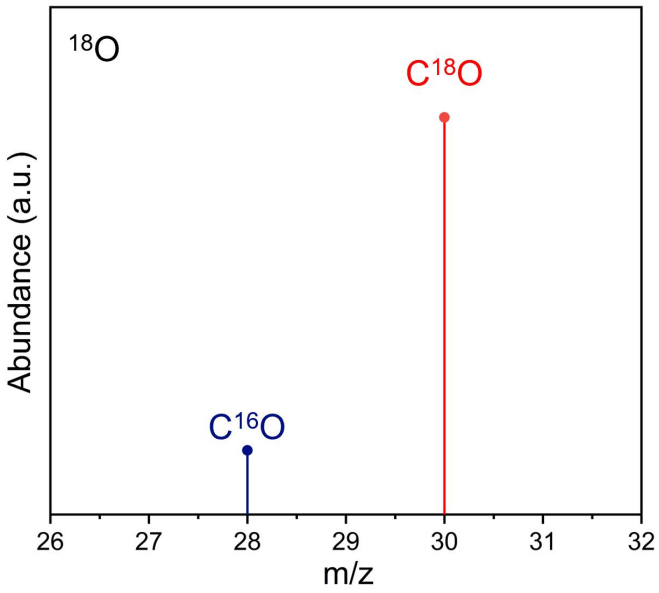

Supplementary Fig. 35. Isotope mass spectrometer (Isotope-MASS) spectra of $C^{16}O$, and $C^{18}O$ from the light-driven DRM reaction of $C^{18}O_2$ over $NiIr_{0.5}/TiO_2$.

(To avoid direct $C^{18}O_2$ scission in isotope-MASS affecting the measurement results, the CO products were pre-separated from the gas sample using a cold trap device before detection.)

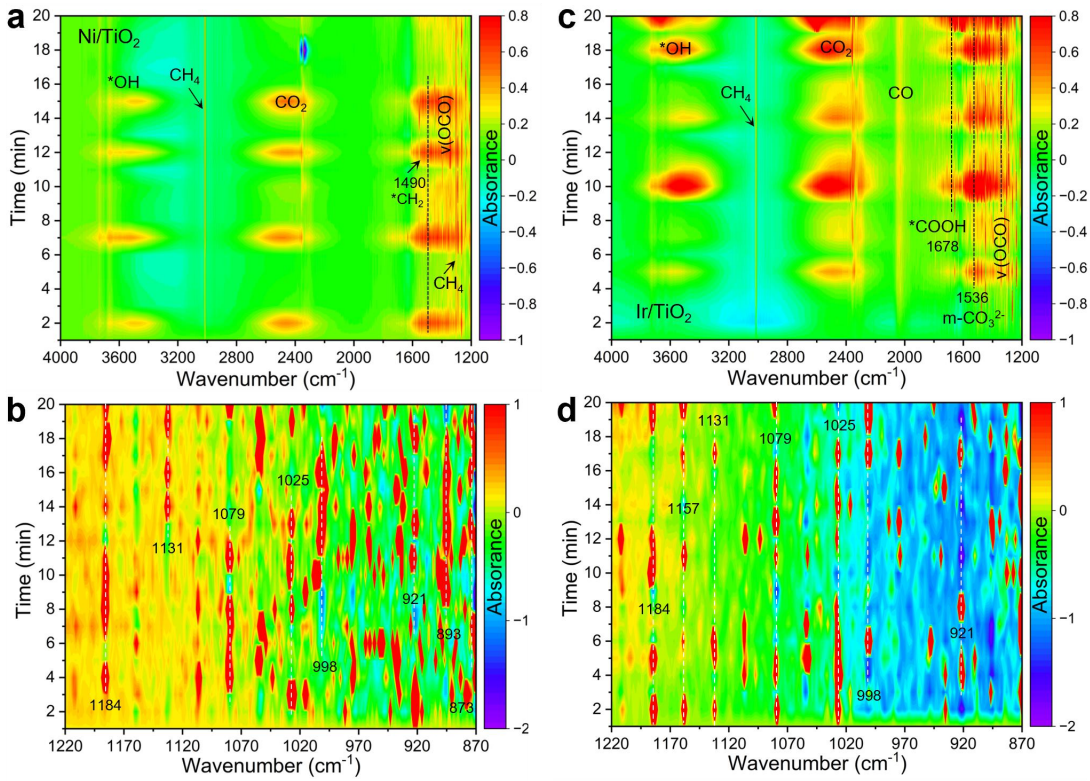

Supplementary Fig. 36. *In-situ* SR-DRIFTS of monometallic-loaded TiO_2 samples during light-driven DRM conditions. *In-situ* SR-DRIFTS in a range of (a) 4000-1200 cm^{-1} and (b) below 1200 cm^{-1} of Ni/TiO_2. *In-situ* SR-DRIFTS in a range of (c) 4000-1200 cm^{-1} and (d) below 1200 cm^{-1} of Ir/TiO_2. (Light intensity: 3.89 W cm^{-2}; Feed gas: CH_4:CO_2:Ar =1:1:8.)

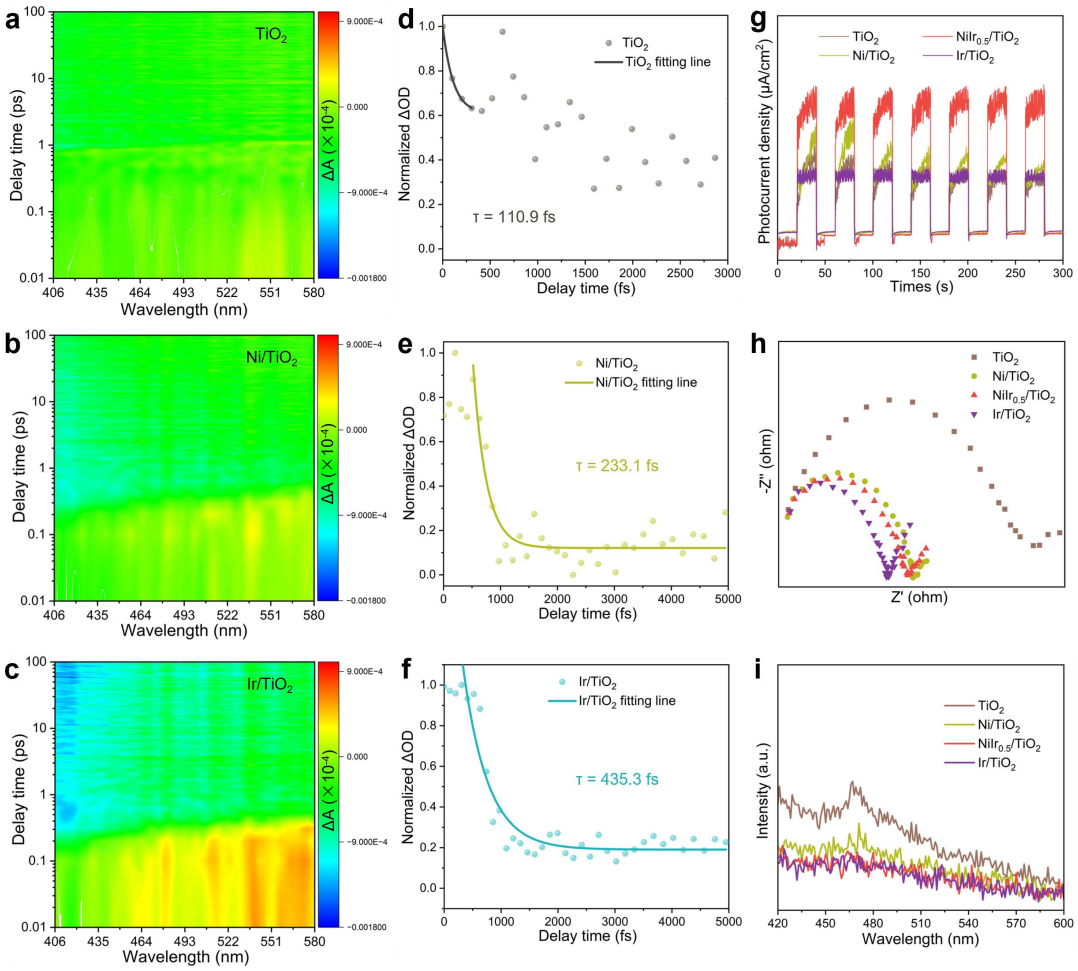

Supplementary Fig. 37. Photoexcited charge dynamics analysis. 2D TA spectroscopy mapping of (a) TiO_2, (b) Ni/TiO_2, and (c) Ir/TiO_2. Normalized TA decay kinetics of (d) TiO_2, (e) Ni/TiO_2, and (f) Ir/TiO_2 at 560 nm. (g) Transient photocurrent responses, (h) Electrochemical impedance spectra, and (c) photoluminescence emission spectra of TiO_2, Ni/TiO_2, $NiIr_{0.5}/TiO_2$, and Ir/TiO_2.

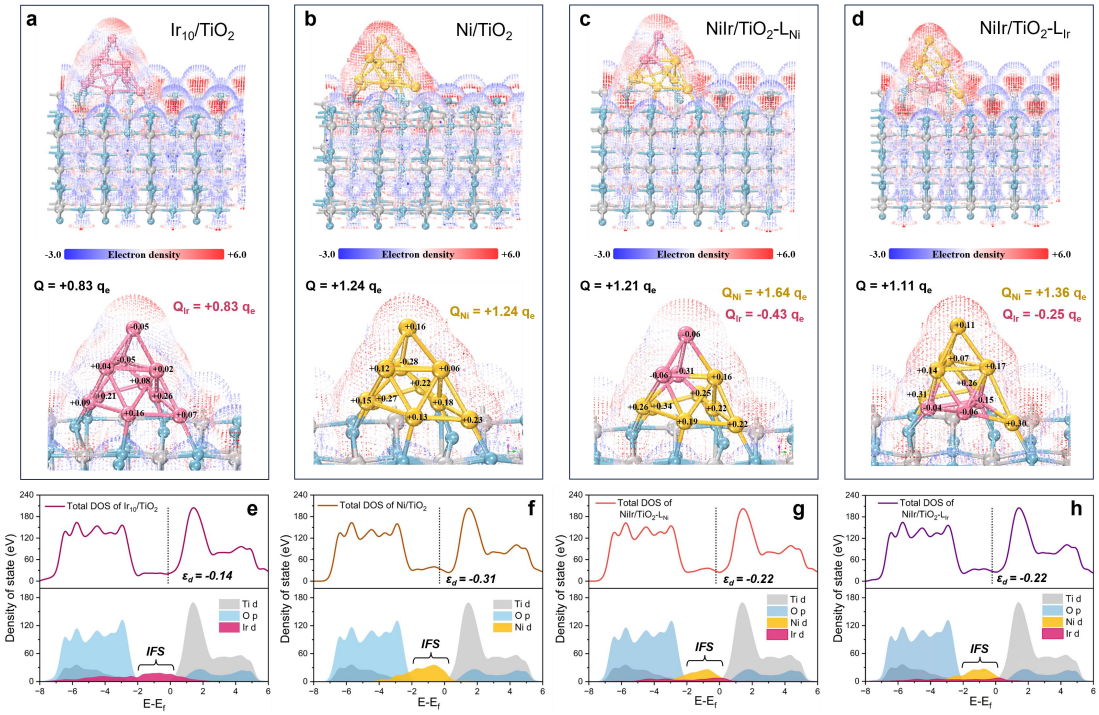

Supplementary Fig. 38. Photoexcited charge dynamics analysis. Electron-density distribution and the corresponding Mulliken charges analysis of (a) Ir_{10}/TiO_2, (b) Ni/TiO_2, (c) $NiIr/TiO_2$-L_{Ni}, and (d) $NiIr/TiO_2$-L_{Ir}. The isosurface level is 0.05 e $Å^{-3}$. Ir, Ni, Ti, and O atoms are shown in pink, yellow, grey, and blue colors, respectively. Calculated density of states for (e) Ir_{10}/TiO_2, (f) Ni/TiO_2, (g) $NiIr/TiO_2$-L_{Ni}, and (h) $NiIr/TiO_2$-L_{Ir}.

Supplementary Note 7.

Electron-density distribution analysis (Supplementary Fig. 38a-d) reveal pronounced electron localization at interfacial regions and metal clusters, demonstrating enhanced electronic polarization that facilitates preferential adsorption and activation of CH_4 and CO_2. Mulliken charge analysis quantifies distinct interfacial charge redistribution patterns: The Ni cluster in Ni/TiO_2 exhibits the highest charge transfer ($Q = +1.24\ q_e$) to the TiO_2 support, while the Ir cluster in Ir_{10}/TiO_2 shows minimal charge exchange ($Q = +0.83\ q_e$), confirming Ni's superior ability to interact with TiO_2. Upon forming the NiIr alloy in $NiIr/TiO_2$-L_{Ni}, the total charge transfer slightly decreases ($Q = +1.21\ q_e$), yet a remarkable charge polarization emerges between Ni ($Q = +1.64\ q_e$) and Ir ($Q = -0.43\ q_e$). This charge disparity directly evidences Ni→Ir electron transfer during alloy formation, consistent with in situ XAS and NAP-XPS observations. In contrast, the $NiIr/TiO_2$-L_{Ir} analog with interfacial Ir substitution exhibits reduced charge transfer, highlighting Ni's critical role as an electron-transfer mediator. Density of states (DOS) calculations (Supplementary Fig. 38e-h) resolve the electronic origins of these phenomena: The valence band of TiO_2 primarily comprises O 2p orbital, while the conduction band derives from Ti 3d states. Interface states (IFS) emerge in metal-modified systems via hybridization between Ni 3d/Ir 5d and O 2p orbitals. Ni/TiO_2 exhibits the strongest IFS intensity but the lowest d-band center ($\varepsilon_d = -0.31$ eV), whereas Ir_{10}/TiO_2 shows weak IFS with a highest d-band center ($\varepsilon_d = -0.14$ eV). The $NiIr/TiO_2$-LNi architecture optimally balances these properties—moderate IFS intensity and d-band center (ε_d =-0.22 eV)—thereby enhancing reactant adsorption while preventing intermediate over-stabilization.

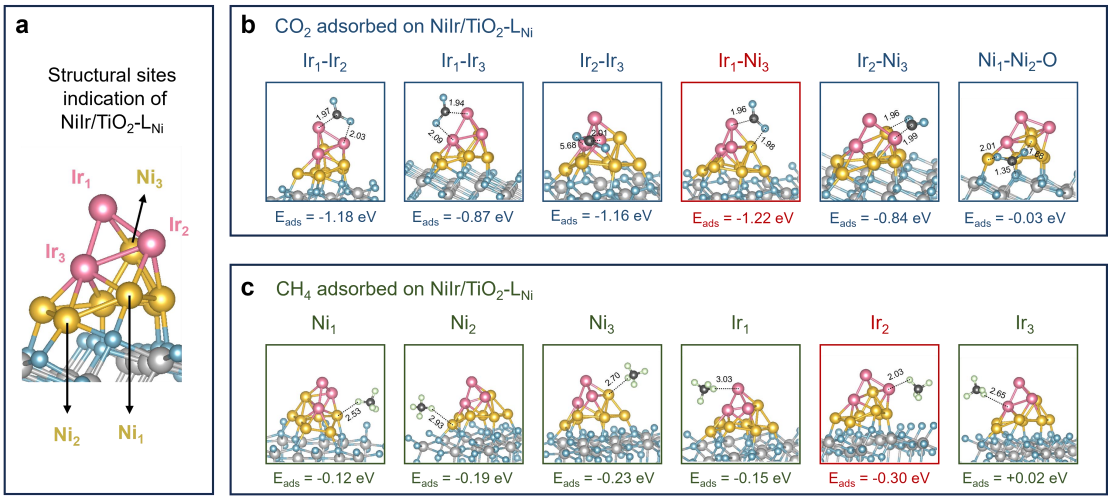

Supplementary Fig. 39. DFT-optimized adsorption configurations for CO_2 and CH_4 adsorption on different sites of NiIr/TiO_2-L_{Ni}.

Since the C=O bonds in CO_2 have already been bent and activated during the adsorption process, the overall adsorption energy of CO_2 is lower than that of CH_4. (Ir, Ni, Ti, and O atoms are shown in pink, yellow, grey, and blue colors, respectively.)

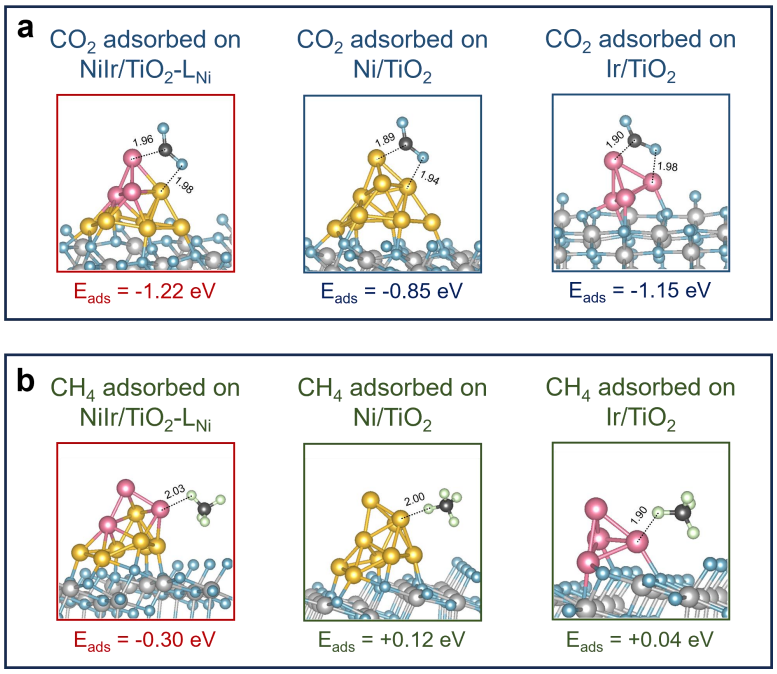

Supplementary Fig. 40. DFT-optimized CO_2 and CH_4 adsorption configurations on $NiIr/TiO_2$-L_{Ni}, Ni/TiO_2, and Ir/TiO_2 models.

(Ir, Ni, Ti, and O atoms are shown in pink, yellow, grey, and blue colors, respectively.)

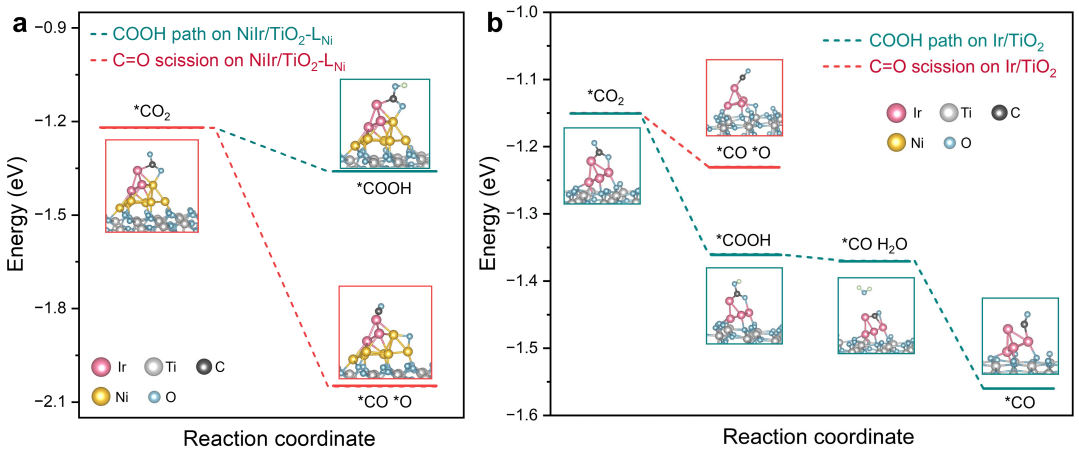

Supplementary Fig. 41. Reaction energy profiles for comparison of direct C=O scission and COOH pathways. (a) NiIr/TiO_2-L_{Ni} model. (b) Ir/TiO_2 model. (Ir, Ni, Ti, and O atoms are shown in pink, yellow, grey, and blue colors, respectively.)

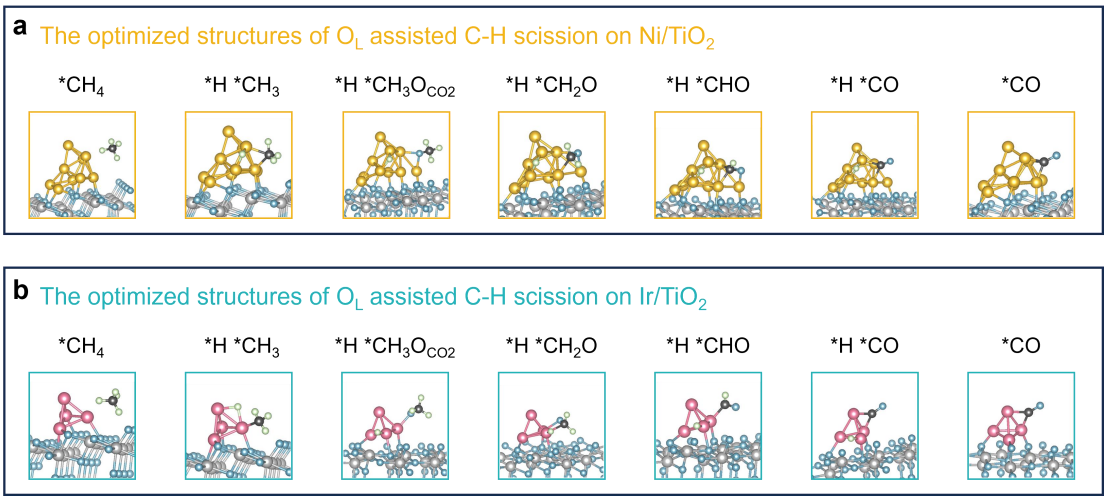

Supplementary Fig. 42 DFT-optimized reaction configurations in Figure 5c. (a) Ni/TiO_2 model. (b) Ir/TiO_2 model. (Ir, Ni, Ti, and O atoms are shown in pink, yellow, grey, and blue colors, respectively.)

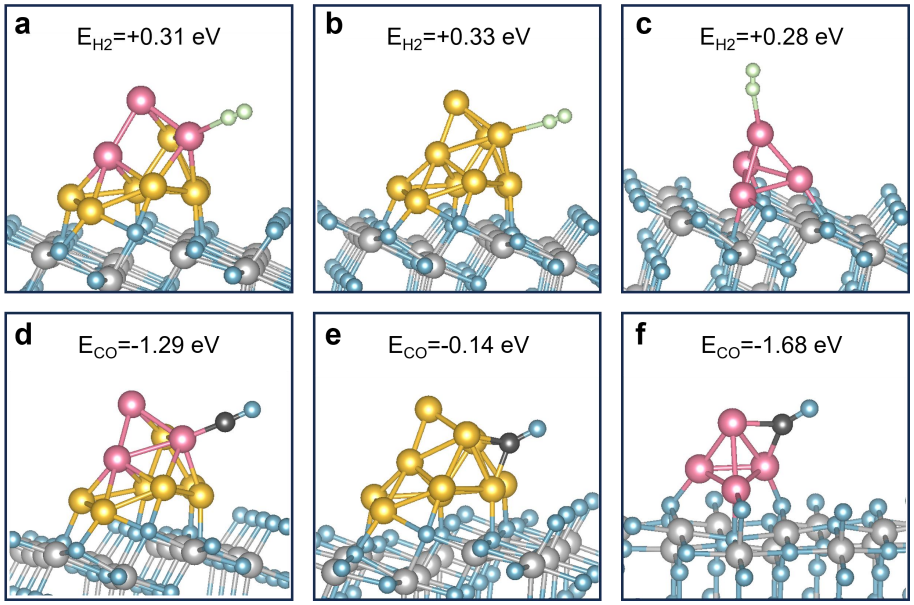

Supplementary Fig. 43 DFT-optimized configurations for productions adsorption. H_2 adsorption configurations on (a) NiIr/TiO_2-L_{Ni}, (b) Ni/TiO_2 model, and (c) Ir/TiO_2 model. CO adsorption configurations on (d) NiIr/TiO_2-L_{Ni}, (e) Ni/TiO_2 model, and (f) Ir/TiO_2 model. (Ir, Ni, Ti, and O atoms are shown in pink, yellow, grey, and blue colors, respectively.)

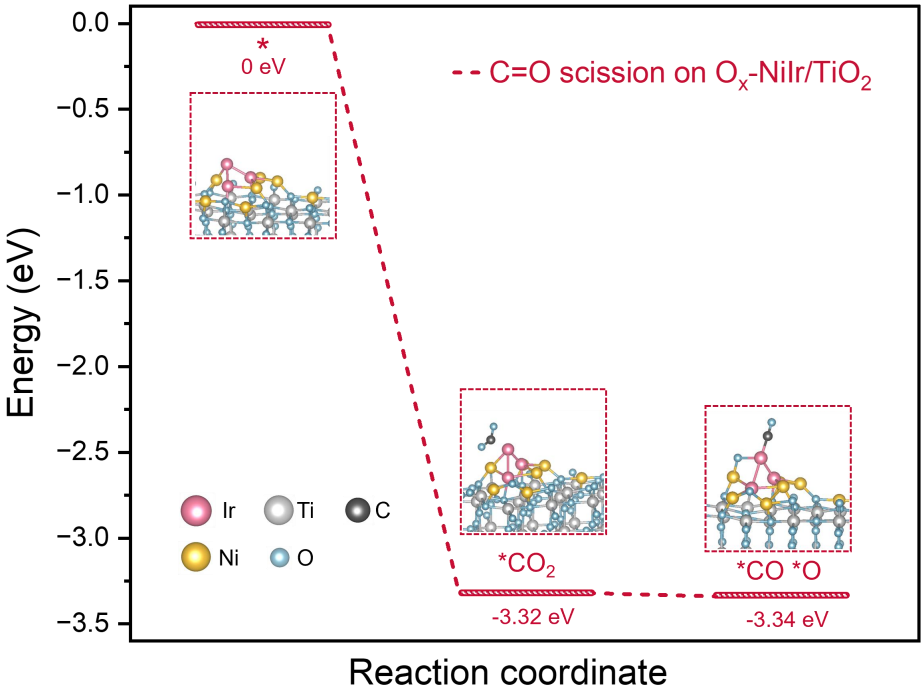

Supplementary Fig. 44 Reaction energy profiles for C=O scission of CO_2 on O_x-NiIr/TiO_2 model. (Ir, Ni, Ti, and O atoms are shown in pink, yellow, grey, and blue colors, respectively.)

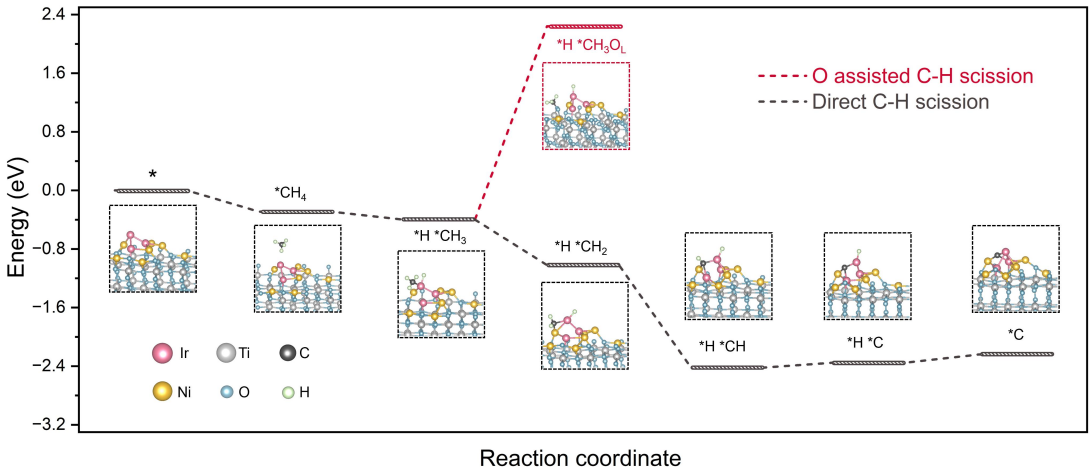

Supplementary Fig. 45 Reaction energy profiles for C-H scission of CH_4 on O_x-NiIr/TiO_2 model. (Ir, Ni, Ti, and O atoms are shown in pink, yellow, grey, and blue colors, respectively.)

Supplementary Table 1. ICP-AES elemental analysis for various samples.

Metal/TiO_2	M_1 contents [a]		M_2 contents [a]	
	wt.%	mmol/g	wt.%	mmol/g
Ir/TiO_2 [b]	0.97	0.050	/	/
0.5% Ir/TiO_2 [b]	0.43	0.022	/	/
$NiIr_{1.0}/TiO_2$ [c]	0.74 (Ni)	0.12 (Ni)	1.05 (Ir)	0.055 (Ir)
$NiIr_{0.75}/TiO_2$ [c]	0.72 (Ni)	0.12 (Ni)	0.94 (Ir)	0.049 (Ir)
$NiIr_{0.5}/TiO_2$ [c]	0.72 (Ni)	0.12 (Ni)	0.87 (Ir)	0.045 (Ir)
$NiIr_{0.25}/TiO_2$ [c]	0.69 (Ni)	0.12 (Ni)	0.59 (Ir)	0.031 (Ir)
$NiIr_{0.15}/TiO_2$ [c]	0.74 (Ni)	0.12 (Ni)	0.38 (Ir)	0.020 (Ir)
$NiIr_{0.05}/TiO_2$ [c]	0.73 (Ni)	0.12 (Ni)	0.07 (Ir)	0.004 (Ir)
Ni/TiO_2 [b]	0.98	0.17	/	/
$NiAu_{0.5}/TiO_2$	0.74 (Ni)	0.12 (Ni)	0.79 (Au)	0.040 (Au)
$NiPd_{0.5}/TiO_2$	0.70 (Ni)	0.12 (Ni)	0.62 (Pd)	0.058 (Pd)
$NiPt_{0.5}/TiO_2$	0.78 (Ni)	0.13 (Ni)	0.85 (Pt)	0.044 (Pt)
$NiRu_{0.5}/TiO_2$	0.72 (Ni)	0.12 (Ni)	0.65 (Ru)	0.064 (Ru)
$CoIr_{0.5}/TiO_2$	0.76 (Co)	0.13(Co)	0.89 (Ir)	0.046 (Ir)
$FeIr_{0.5}/TiO_2$	0.71 (Fe)	0.13 (Fe)	0.75 (Ir)	0.039 (Ir)
$PtIr_{0.5}/TiO_2$	1.06 (Pt)	0.054 (Pt)	0.73 (Ir)	0.038 (Ir)
$NiIr_{0.5}/SiO_2$	0.73 (Ni)	0.12 (Ni)	0.82 (Ir)	0.043 (Ir)

[a] Analyzed by the ICP-AES method.

[b] In Ni/TiO_2 and Ir/TiO_2, the theoretical loading amount of Ni or Ir relative to TiO_2 is 1 wt.%. In 0.5% Ir/TiO_2, the theoretical loading of Ir relative to TiO_2 is 0.5 wt.%.

[c] In $NiIr_x/TiO_2$, x represents the theoretical atomic ratio of Ir to Ni.

Note that the actual Ir loading amounts of in Ir/TiO_2 is similar to that in $NiIr_{0.75}/TiO_2$, and the actual Ir loading amounts in 0.5% Ir/TiO_2 is similar to that in $NiIr_{0.15}/TiO_2$.

Supplementary Table 2. H_2-O_2 titration results for $NiIr_{0.5}/TiO_2$.

Treatment/Loop	10%H_2/Ar
Blend	5%O_2/He
Quantitative loop volume	0.5199 ml/STP
Metal dispersion	38.31%

Supplementary Table 3. Comparison of representative systems for photothermal and thermal DRM reaction.

Sample	Light Intensity ($W\ cm^{-2}$)	Temp-erature (°C)[a]	Catalyst weight (mg)	Feed gas composition	Production rates			TOF (s^{-1})	LTFE	Ref.
					H_2 ($mmol\ g_{cat}^{-1}\ h^{-1}$)	CO ($mmol\ g_{cat}^{-1}\ h^{-1}$)	H_2/CO			
$NiIr/TiO_2$	3.89	506	5	CO_2:CH_4:Ar =1:1:0 20 mL/min	5025	5816	0.86	23 (NiIr)	25%	This work
				CO_2:CH_4:Ar =1:1:8 20 mL/min	1244	1268	0.98	5.5 (NiIr)	4.8%	
$Cu_{19.8}Ru_{0.2}$/ MgO-Al_2O_3	19.2	727	1.5	CO_2:CH_4=1:1 8 mL/min	~1980	~1980	~1.00	3.3[b] (CuRu)	15%	[13]
Ni/CeO_2	36.34	807	50	CO_2:CH_4:Ar ≈1:1:8 30 mL/min	391.8	376.2	1.04	0.90[b] (Ni)	11%	[14]
Ru_{NPs}/TiO_2-H_2	12	450	5	CO_2:CH_4:Ar =8:8:84 50 mL/min	645.5	708.4	0.91	6.8[b] (Ru)	NR	[15]
Pt/La_2O_3	19.42	700	5	CO_2:CH_4:Ar =8:8:84 90 mL/min	1284.5	1443.3	0.89	5.3[b] (Pt)	8%	[16]
Rh/Ce_xWO_3	2.85	440	50	CO_2:CH_4:Ar =1:1:3 50 mL/min	~47.3	~68.0	~0.70	0.36[b] (Rh)	4.6%	[17]
Ni/TiO_2-650	15	620	10	CO_2:CH_4:Ar =12:12:1 87.45 mL/min	4016	5686	0.71	3.4[b] (Ni)	29.9%	[18]
Rh/TiO_2-B nanobelts	150 W Hg-Xe lamp	403	10	CO_2:CH_4:Ar =1:1:98 10 mL/min	21.5	21.2	1.01	0.04 (Rh)	NR	[19]
$Ru/SrTiO_3$	NR	600	150	CO_2:CH_4:N_2 =9:9:7 45 mL/min	320.29	388.99	0.82	20[b] (Ru)	NR	[20]
Ni_{SA}/CeO_2	2.4	472	25	CO_2:CH_4:Ar =1:1:3 20 mL/min	66.5	59.7	1.11	0.13[b] (Ni)	1.6%	[21]
$Rh/LaNiO_3$	3.5	440	50	CO_2:CH_4:Ar =1:1:3 50 mL/min	166.9	244.8	0.68	5.1[b] (Rh)	10.7%	[22]
Pt-Si-CeO_2	1.78	600	10	CO_2:CH_4:Ar =1:1:8	90	154	0.58	8.5[b] (Pt)	NR	[23]

				14 mL/min						
CoNiRuRhPd /$SrTiO_3$	4.0	560	5	CO_2:CH_4:Ar =1:1:8 20 mL/min	358.8	368.0	0.98	3.2[b] (alloy)	2.1	[24]
2Ni/HAP-Ce[c]	/	750	50	CO_2:CH_4:He =1:1:3 50 mL/min	~964.3	~1017	~0.95	15.6 (Ni)	/	[25]
Ni/La_2O_3-LOC[c]	/	700	100	CO_2:CH_4:He =15:15:70 100 mL/min	~950.4	~1092	0.87	12.8 (Ni)	/	[26]
Ni_1/CoCe[c]	/	800	100	CO_2:CH_4:Ar =1:1:3 50 mL/min	~482	~507	~0.95	14.5 (Ni)	/	[27]
Ni/SiO_2@SiO_2-9nm[c]	/	800	100	CO_2:CH_4:N_2 =9:9:2 21 mL/min	~109.3	~182.2	~0.6	21.2 (Ni)	/	[28]

[a] Temperature here refers to the maximum value of the measured temperature or the additional heating temperature at the corresponding condition.

[b] These TOF values (s^{-1}) were not directly reported and were calculated using available parameters. Specifically, the active site dispersion required for TOF calculation was estimated via the relationship between the average size and dispersion of metal nanoparticles measured in this work.

[c] Thermal catalytic system.

NR: not reported.

Supplementary Table 4. Curvefit parameters[a] for Ir L_3-edge EXAFS of $NiIr_{0.5}/TiO_2$, Ir/TiO_2 during light DRM reaction, and Ir foil.

Samples	Path	Coordination number (CN)	Radial distance/Å	σ^2/Å^2 [c]	ΔE_0[d]	R factor
Ir foil	Ir-Ir	8[b]	2.69±0.01	0.002	6.42	0.008
$Ni_{1.0}Ir_{0.5}$/TNS-light	Ir-Ni	2.0±0.5	2.34±0.05	0.008	4.69	0.020
	Ir-Ni	5.8±0.7	2.57±0.03	0.010		
Ir/TNS-light	Ir-O	1.1±0.4	1.98±0.02	0.003	6.86	0.016
	Ir-Ir	5.9±0.9	2.67±0.04	0.006		

[a] S_0^2 was set to 1.0, according to the experimental EXAFS fit of Ir foil reference by fixing CN as the known crystallographic value. Data ranges: $3 \leq k \leq 10.5$ Å^{-1}, $1.0 \leq R \leq 3.0$ Å. [b] These parameters were constrained for reducing the number of variables. [c] σ^2: Debye-Waller factors; [d] ΔE_0: the inner potential correction. ΔE_0 was refined as a global fit parameter.

Supplementary Table 5. Curvefit parameters[a] for Ni K-edge EXAFS of $NiIr_{0.5}/TiO_2$, Ni/TiO_2 during light DRM reaction, and Ni foil.

Samples	Path	Coordination number (CN)	Radial distance/Å	σ^2/Å^2 [c]	ΔE_0[d]	R factor
Ni foil	Ni-Ni	8[b]	2.49±0.01	0.006	4.36	0.008
$Ni_{1.0}Ir_{0.5}$/TNS-light	Ni-O	3.4±0.8	2.03±0.05	0.006	4.70	0.023
	Ni-Ni	2.9±0.7	2.50±0.08	0.006		
	Ni-Ir	3[b]	2.57±0.00			
Ni/TNS-light	Ni-Ni	8.0±0.7	2.49±0.01	0.005	4.58	0.012

[a] S_0^2 was set to 1.0, according to the experimental EXAFS fit of Ni foil reference by fixing CN as the known crystallographic value. Data ranges: $3 \leq k \leq 10.5$ Å^{-1}, $1.0 \leq R \leq 3.0$ Å. [b] These parameters were constrained for reducing the number of variables. [c] σ^2: Debye-Waller factors; [d] ΔE_0: the inner potential correction. ΔE_0 was refined as a global fit parameter.

Supplementary Reference

1 Kresse, G. & Furthmüller, J. Efficiency of ab-initio total energy calculations for metals and semiconductors using a plane-wave basis set. *Comput. Mater. Sci.* **6**, 15-50 (1996).

2 Kresse, G. & Furthmüller, J. Efficient iterative schemes for ab initio total-energy calculations using a plane-wave basis set. *Phys. Rev. B* **54**, 11169-11186 (1996).

3 Selcuk, S. & Selloni, A. Facet-dependent trapping and dynamics of excess electrons at anatase TiO_2 surfaces and aqueous interfaces. *Nat. Mater.* **15**, 1107-1112 (2016).

4 Perdew, J. P., Burke, K. & Ernzerhof, M. Generalized gradient approximation made simple. *Phys. Rev. Lett.* **77**, 3865-3868 (1996).

5 Neese, F. Software update: the ORCA program system, version 4.0. *WIREs Comput. Mol. Sci.* **8**, e1327 (2018).

6 Lu, T. & Chen, F. Multiwfn: A multifunctional wavefunction analyzer. *J. Comput. Chem.* **33**, 580-592 (2012).

7 Humphrey, W., Dalke, A. & Schulten, K. VMD: Visual molecular dynamics. *J. Mol. Graph.* **14**, 33-38 (1996).

8 Ding, K. *et al.* A general synthesis approach for supported bimetallic nanoparticles via surface inorganometallic chemistry. *Science* **362**, 560-564 (2018).

9 Luo, S. *et al.* Light-induced dynamic restructuring of Cu active sites on TiO_2 for low-temperature H_2 production from methanol and water. *J. Am. Chem. Soc.* **145**, 20530-20538 (2023).

10 Zou, S. *et al.* Manufacturing single-atom alloy catalysts for selective CO_2 hydrogenation via refinement of isolated-alloy-islands. *Angew. Chem. Int. Ed.* **64**, e202412835 (2025).

11 Zhou, J. *et al.* Interfacial compatibility critically controls Ru/TiO_2 metal-support interaction modes in CO_2 hydrogenation. *Nat. Commun.* **13**, 327 (2022).

12 Li, X. *et al.* Controlling CO_2 hydrogenation selectivity by metal-supported electron transfer. *Angew. Chem. Int. Ed.* **59**, 19983-19989 (2020).

13 Zhou, L. *et al.* Light-driven methane dry reforming with single atomic site antenna-reactor plasmonic photocatalysts. *Nat. Energy* **5**, 61-70 (2020).

14 Zhang, Q. *et al.* Novel photoactivation promoted light-driven CO_2 reduction by CH_4 on Ni/CeO_2 nanocomposite with high light-to-fuel efficiency and enhanced stability. *Appl. Catal. B Environ.* **239**, 555-564 (2018).

15 Li, Q. *et al.* Suppressive strong metal-support interactions on ruthenium/TiO_2 promote light-driven photothermal CO2 reduction with methane. *Angew. Chem. Int. Ed.* **62**, e202300129 (2023).

16 Gao, Y. *et al.* Light-driven efficient dry reforming of methane over Pt/La_2O_3 with long-term durability. *J. Mater. Chem. A* **10**, 16016-16028 (2022).

17 Yang, Y. *et al.* Light-induced redox looping of a rhodium/$CeWO_3$ photocatalyst for highly active and robust dry reforming of methane. *Angew. Chem. Int. Ed.* **61**, e202200567 (2022).

18 He, Z. *et al.* Engineering an Ni-TiO_x interface for highly active and durable solar-driven dry reforming of methane. *Chem Catal.* **4**, 101040 (2024).

19 Kushida, M., Yamaguchi, A. & Miyauchi, M. Photocatalytic dry reforming of methane by rhodium supported monoclinic TiO_2-B nanobelts. *J. Energy Chem.* **71**, 562-571 (2022).

20 Tang, Y. *et al.* Enhanced dry reforming of CO_2 and CH_4 on photothermal catalyst $Ru/SrTiO_3$. *Appl. Catal. B Environ.* **338**, 123054 (2023).

21 Rao, Z. *et al.* Light-reinforced key intermediate for anticoking to boost highly durable methane dry reforming over single atom Ni active sites on CeO_2. *J. Am. Chem. Soc.* **145**, 24625-24635 (2023).

22 Yao, Y. *et al.* Highly efficient solar-driven dry reforming of methane on a Rh/$LaNiO_3$ catalyst through a light-induced metal-to-metal charge transfer process. *Adv. Mater.* **35**, 2303654 (2023).

23 Pan, F. *et al.* A novel photo-thermochemical approach for enhanced carbon dioxide reforming of methane. *ChemCatChem* **10**, 940-945 (2018).

24 Xiong, H. *et al.* Highly efficient and selective light-driven dry reforming of methane by a carbon exchange mechanism. *J. Am. Chem. Soc.* **146**, 9465-9475 (2024).

25 Akri, M. *et al.* Atomically dispersed nickel as coke-resistant active sites for methane dry reforming. *Nat. Commun.* **10**, 5181 (2019).

26 Li, X. *et al.* Dry reforming of methane over Ni/La_2O_3 nanorod catalysts with stabilized Ni nanoparticles. *Appl. Catal. B Environ.* **202**, 683-694 (2017).

27 Wu, J. *et al.* Engineering the oxygen vacancies enables Ni single-atom catalyst for stable and efficient C-H activation. *Appl. Catal. B Environ.* **314**, 121516 (2022).

28 Han, J. W., Park, J. S., Choi, M. S. & Lee, H. Uncoupling the size and support effects of Ni catalysts for dry reforming of methane. *Appl. Catal. B Environ.* **203**, 625-632 (2017).